UNIVERSITÀ DEGLI STUDI DI PADOVA

DEPARTMENT OF INFORMATION ENGINEERING

MASTER'S THESIS IN

ELECTRONIC ENGINEERING

Characterization of a grating monochromator for the spectral selection of extreme-ultraviolet ultrafast pulses

Supervisor:

Dr. Luca Poletto

Co-supervisors:

Dr. Fabio Frassetto

Eng. Paolo Miotti

Author: Nicola Fabris

Academic Year 2015/2016

Dedico questa tesi ai miei genitori,
che da sempre mi sostengono con affetto...

Contents

Chapter 1

Introduction

High harmonic generation uses a quirk of nonlinear physics to generate frequencies much higher than the second, third, or fourth harmonics produced by conventional nonlinear optics. Directing an ultrashort laser pulse into a suitable gas a burst of coherent light at odd harmonics of the pump-light frequency spanning many octaves is produced. The energy in each harmonic drops at low frequencies, then levels out in a plateau of successive harmonics that have similar energy before eventually dropping to zero at even higher levels, as illustrated in Fig. 1.1.

First demonstrated in the late 1980s, high harmonic generation has become a hot field because it can produce coherent light in the extreme ultraviolet (EUV) and soft X-ray region without the need for a costly and cumbersome accelerator.

Now it's pushing the frontier in ultrafast physics, where researchers are seeking to move from attoseconds to zeptoseconds. And in a new experiment, researchers have used high harmonic techniques to produce EUV femtosecond frequency combs powerful enough to perform previously impossible spectroscopic measurements.

Extremely short and intense laser pulses produce high-order harmonics when they interact with a noble gas. The strong electric field near the peak of the pulse pulls an electron from the atom's outer shell, but the direction of the electric field changes before it ionizes the atom. The electron then drops back to a lower-energy state in the atom, releasing it's extra energy in a series of odd harmonics of the pump laser frequency.

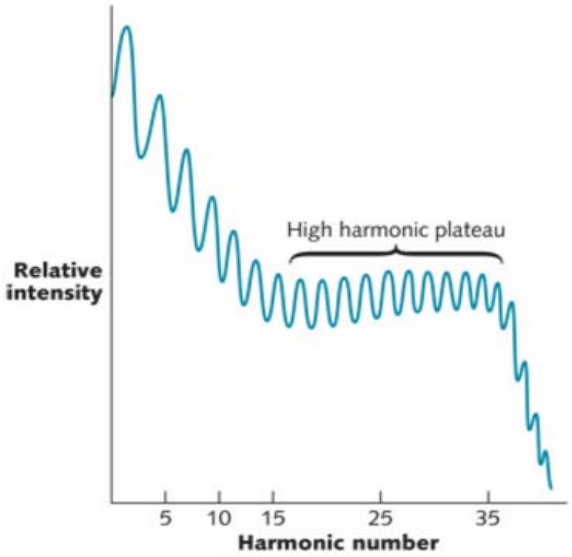

Figure 1.1: High harmonic generation in a noble gas generates peaks at odd harmonics. Power drops at higher harmonic numbers up to a point, then levels out in a plateau before dropping at much higher harmonics. Actual measurements of harmonic power may include more features, such as a low-intensity zone between the lowest harmonics and the plateau.

When the pump intensity is above 10^{13} W/cm^2, intensity of the emitted light stays nearly constant across a number of harmonics before dropping sharply at higher harmonics.

Features such as what harmonics are generated, the harmonic power, and the cutoff wavelength depend on the gas used, and on characteristics of the pump light including wavelength, pulse duration, and pulse repetition rate. [1]

It has been demonstrated that longer pump wavelengths can produce higher harmonics despite their lower photon energy. This happens because electric fields change more slowly at longer pump wavelengths, giving the fields more time to accelerate electrons, so they have more energy to emit when they recombine with the atom. For example, the cutoff wavelength for argon excited by an 800 nm Ti:sapphire laser is about 25 nm (50 eV), but pumping at 1.4 μm yielded wavelengths as short as 12 nm (100 eV). [2]

Although high harmonic power is low, it is adequate for many research applications in the EUV and soft X-ray region, where conventional lasers are not available, and synchrotron sources are costly, and complex. Early high harmonic systems were built around modelocked Ti:sapphire lasers with repetition rates of a few hertz to several thousand hertz, followed by regenerative amplifiers to boost their output power. Developers are now fine-tuning their systems for other specific applications.
Driving high harmonic generation with femtosecond lasers modelocked at high repetition rates produces rather different results-frequency combs in the EUV. When the driver pulses are repeated steadily at high rates the high harmonic waves they generate interfere with each other to produce frequency combs. The result is not a single frequency comb spanning the entire EUV, but a series of shorter combs; each one a series of closely spaced teeth in a different harmonic band, as shown in Fig. 1.2.

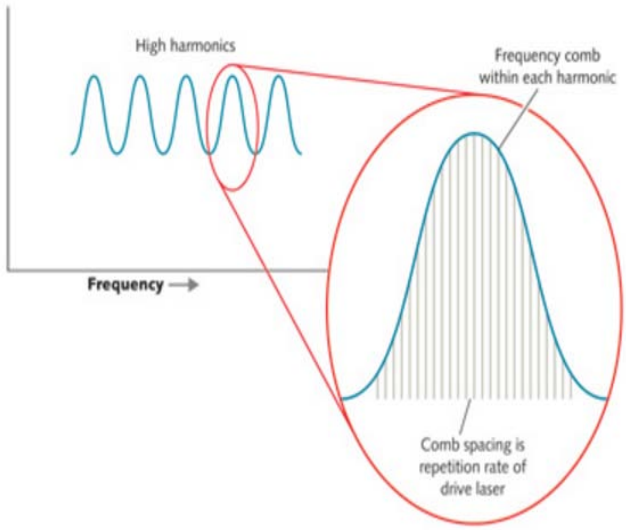

Figure 1.2: Each high harmonic peak contains frequency comb lines, with their frequency separated by the repetition rate of the femtosecond laser driving the high harmonic generator. Typically 10˙000 to 1 million comb lines fall within one harmonic peak.

A simple modelocked femtosecond laser does not emit powerful enough pulses for ordinary high harmonic generation. A recent experiment has shown that amplification and pulse compression of pulses from a Yb:KGW laser modelocked at 20.8 MHz can produce high harmonics when focused into a xenon jet, but so far powers are limited to nanowatts. However, the power can be stepped up by coupling the laser pulses into a femtosecond enhancement cavity and moving the harmonic generation into the cavity, as shown in Fig. 1.3. Stabilizing the cavity and adjusting it so its cavity round-trip time matches that of the laser produces a resonance that enhanced intracavity pulse energy by nearly a factor of 1000. Placing a high harmonic generation cell inside the cavity took advantage of those higher-energy drive pulses, yielding a train of high harmonic pulses at the same repetition rate as the driver.

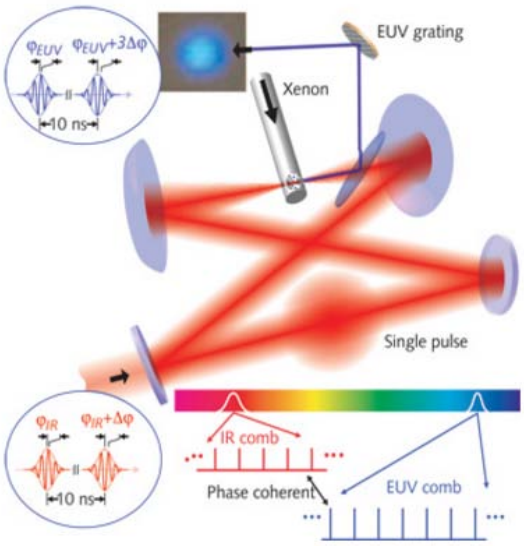

Figure 1.3: Pulse train from an external modelocked femtosecond laser is coupled into an enhancement cavity for high harmonic generation. Matching the cavity to the pulse train resonantly enhances the power of the circulating single pulse, which is focused onto xenon gas to generate high harmonics that are phase coherent with the drive laser.

The resulting EUV frequency comb offers a powerful spectroscopic probe. However, the output power in each harmonic is divided among 10^4 to 10^6 teeth, so each tooth has little power. At visible wavelengths, frequency combs can calibrate more powerful lasers for spectroscopic measurements.

Spectroscopic applications of High-order laser harmonics (HHs) often require the spectral selection of a single harmonic in a narrow XUV band, especially for experiments aimed to understand the electronic structures of materials, where multiple orders of HHs have to be filtered out. Although multilayer mirrors are the simplest optical elements for the spectral selection of one harmonic order and are successfully employed for HHs and synchrotron beam lines, they they lack of broad-band tunability and may give a poor contrast ratio between adjacent harmonics. [3]

A grating monochromator, although more complex than a single multilayer mirror, gives both tunability in a broad range of harmonics and high spectral selectivity. Unfortunately, it introduces a stretch of the pulse duration because of the **pulse-front tilt**, compromising the ultrafast duration of HHs, as schematically shown in Fig. 1.4.

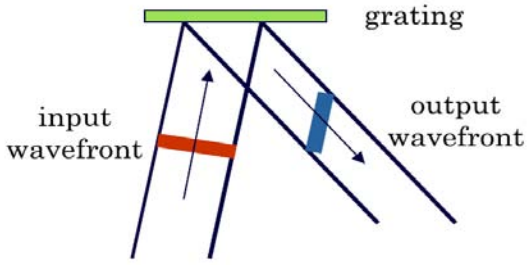

Figure 1.4: Pulse front-tilt given by a diffraction grating. The tilt of the output wavefront is $Nm\lambda$, where N is the number of illuminated grooves, m is the diffraction order, λ is the wavelength.

This effect, although almost negligible in the picosecond or longer time scale, may completely alter the temporal duration of the XUV pulse in the femtosecond regime. Nevertheless, it is possible to design grating monochromators that do not alter the temporal duration of ultrafast pulses by using two gratings in a time-delay compensated configuration,

where the second grating compensates for the front tilt and for the spectral spread introduced by the first one [4, 5]. Pulses as short as 8–10 fs have been measured at the output of double-grating monochromators in the 20–45 nm spectral region. [6, 7] The main drawback of these configurations is the use of two gratings that increase the complexity of the instrument and reduce the efficiency.

The choice between the two options has to be performed as a trade-off between efficiency, that are maximized in the single-grating design, and temporal resolution, that is maximized in the two-grating design.

Two different grating configurations can be adopted for grazing-incidence diffraction from a single grating: **the classical diffraction mount (CDM) and the off-plane mount (OPM)**. We discuss the advantages and drawbacks of both mountings for application to the spectral selection of ultrafast pulses.

The OPM stage gives fast temporal response and low resolution, while the CDM stage gives slower response and higher resolution.

The OPM stage is used to select the whole bandwidth of a single harmonic for ultrafast pump-probe experiments, while the CDM stage is used to increase the spectral purity of the source beyond the limit given by the bandwidth of the single harmonic, at the price of lower photon flux and longer temporal response.

Chapter 2

HHg: High Harmonic Generation

High-order harmonic generation (HHG) is a coherent, highly nonlinear optical process describing the nonlinear interaction between an intense laser pulse and a medium (usually a gas) that results in the generation of harmonics of the driving laser field. This effect can be understood in terms of a nonlinear dependence of the polarization vector of the medium on the incident laser electric field and so the generation of new frequencies, integer multiples of the incident laser frequency, occurs.
Atoms and molecules exposed to a strong laser field emit a light bursts with a sub-femtosecond duration whose spectra has a universal characteristic shape. Coherence, instead, is due to the fact that the HHG signal is a coherent superposition of radiation emission from all the medium points. [8]
There are three significant characteristics that are unique to HHG spectra:

- Intense low-order harmonics where the intensity follows perturbation theory (i.e. the harmonic intensity is proportional to I^q where I is the driving laser intensity and q is the harmonic order).
- A long plateau of harmonics whose intensities are approximately equal.
- A very sharp cutoff where the HHG signal drops rapidly.

The new generated frequencies are in the spectral region between extreme ultraviolet (XUV) and soft X-ray and only odd multiples of the

laser frequency ω appear.
The spectrum that is observed from the high harmonic generation process is the result of two separate processes: generation of harmonic light from a single atom and the subsequent propagation in the medium. The single atom response is accurately predicted by a semi-classical model while the propagation effects are predicted by classical electrodynamics.

2.1 The semi-classical Three-Step Model

We call this approach semi-classical since it uses both quantum and classical mechanics: the ionization by laser field is a quantum phenomenon and the electron motion in the continuum is described classically. The model divide the process in three step, hence is called *Three-Step model* (Fig. 2.1- 2.2).

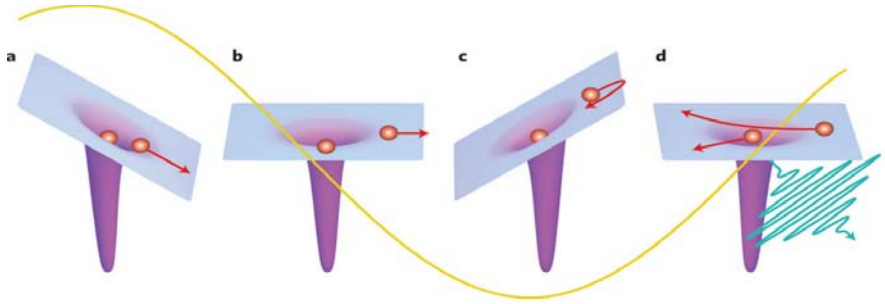

Figure 2.1: An intense femtosecond near-infrared or visible pulse (yellow) extracts an electron wave packet from an atom or molecule. First, the electron is pulled away from the atom near the peak of optical field (**a**) and accelerated (**b**). When the optical field reverses, the electron is driven back (**c**) where it can "recollide" during a small fraction of the laser oscillation cycle (**d**).

1 **Tunnel ionization**: electron extraction occurs through tunnel effect which is in competition with other phenomena.

2 **Propagation**: once ionized, the electron propagates in the continuum following the electric field trend; it is characterized by a

nearly-plane wave function and the more it travels in the continuum the more its wave function broadens.

3 **Recombination**: when the electron is in the continuum it has a certain probability to collide with its parent ion and recombine with it. When it returns in a bound state, owing to energy conservation, the kinetic energy acquired during propagation is converted into one emitted photon; this emission is classically seen as an emission of radiation for Bremsstrahlung after the recollision with the ion.

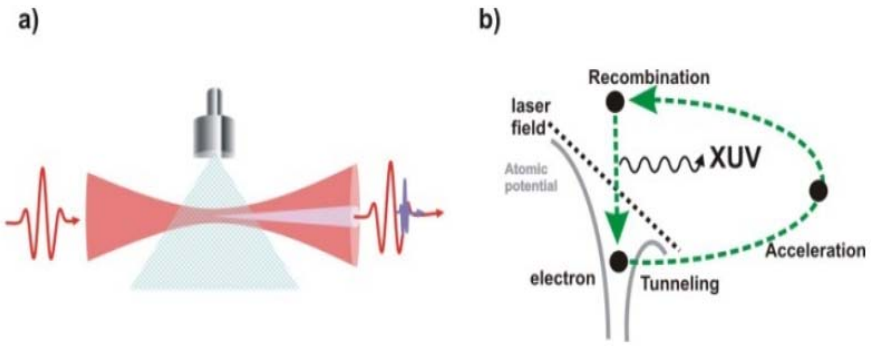

Figure 2.2: a) Sketch of the harmonic generation process. A pulsed laser with high peak power is focused on a gas jet. The harmonics propagate collinearly to the incident beam with a smaller divergence. b) Three steps model of the High Harmonic Generation: atomic ionization, electron acceleration and electron recombination generating the XUV photon.

2.1.1 Tunnel ionization

There are three ways in which an atom can be ionized: multiphoton ionization, tunnel ionization, and above-barrier ionization (Fig. 2.3). The Keldysh parameter in Eq. (2.1) is defined as the ratio of the laser frequency to the tunneling frequency and determines which mechanism is dominant.

$$\gamma = \frac{\omega_{laser}}{\omega_{tunnel}} = \sqrt{\frac{I_p}{2U_p}} \tag{2.1}$$

where I_p is the ionization potential of the atom/ion being ionized and U_p is the ponderomotive energy. The ponderomotive energy is the classical kinetic energy gained by an electron in an oscillating field and is given by Eq. (2.2):

$$U_p = \frac{e^2 E_0^2}{4 m_e \omega_0^2} = \frac{e^2 c \mu_0 I}{2 m_e \omega_0^2} \tag{2.2}$$

where e is the electron charge, E_0 is the electric field strength, m_e is the electron mass, ω_0 is the laser angular frequency, c is the speed of light in a vacuum, μ_0 is the permeability of free space, and I is the laser intensity.
In terms of the laser intensity and wavelength, the ponderomotive energy, in electronvolts, is given by $U_p \approx 9.33 \cdot 10^{-14} I \lambda^2$, with intensity in W/cm^2 and wavelength in μm.

We distinguish two cases:

a) $\gamma >> 1$: it can be used a perturbative approach, **LOPT** (Lower Order Perturbative Theory).

b) $\gamma << 1$: a non perturbative approach is necessary.

An atom exposed to an intense laser field experiences two processes competing with each other: *multi-photon ionization*, which predominate if $\gamma >> 1$, and *tunnel ionization*, which predominate if $\gamma << 1$.
Since U_p depends on the square of the electric field amplitude, the higher is the intensity the lower is the γ parameter, so with relative low intensity the problem can be treated with the perturbation theory at the first order (photon energy much lower than ionization potential), instead for high intensity ($10^{13} - 10^{14}\ W/cm^2$) the perturbative approach can't be used.

In *multi-photon ionization* the electron can reach the continuum absorbing an integer number n of photon such that:

$$n\hbar\omega_0 > I_p. \tag{2.3}$$

In this regime, the effective potential is only slightly modified from the Coulomb potential by the laser field (Fig. 2.3(a)).

In this case the ionization rate (ionization probability per unit of time, so the number of emitted electron per unit of time) is $\Gamma_n = \sigma_n I^n$, where I is the laser intensity and σ_n the cross section of the process. If the electron absorbs more photons than necessary, the exceeding photons give a contribution to the increasing of the electron kinetic energy; this process is known as above threshold ionization (ATI). [9]

At larger laser intensities, $\gamma < 1$, and *tunnel ionization* becomes the dominant mechanism (Fig. 2.3(b)). In this regime, the effective potential is severely distorted by the laser field.
In the tunnel ionization, which occurs if the perturbative approach isn't applicable, the laser electric field distorts the Coulombian field and the atomic potential is deformed. The electron will thus find a potential barrier which it can pass through thanks to tunnel effect. In this case the tunneling ionization rate can be calculated with the ADK (Ammosov, Delone, Krainov) theory [10] in which the tunneling time t_t, the time necessary to the electron for crossing the barrier, is much lower than the oscillation period of the electric field T_0. It can be demonstrated that:

$$\gamma = \frac{t_t}{T_0/2} \tag{2.4}$$

For very short and very intense optical pulses ($\gamma \ll 1$), that is the condition for which the tunnel effect predominates on other ionization forms, is also $t_t \ll T_0$ [11]; t_t is the time that spends the electron to pass through the barrier.
This condition allows to consider the electric field quasi-static and thus the barrier, generated by the field, keep on unmodified for a time long enough to make tunneling process completed.
The hypothesis for which the frequency ω_0 is much lower than $\omega_t = 1/t_t$, so that we can neglect the change of the field during the passage of the electron through the barrier, is called *adiabatic approximation*.
For laser in the spectral region of infrared and visible, like the lasers used for HHG experiments, the approximation is valid.

Finally we obtain the following dependence for the ionization rate:

$$W \approx exp\left(-\frac{\sqrt{m_e}2(2I_p)^{\frac{3}{2}}}{3\hbar eE}\right) \tag{2.5}$$

Indeed W depends on the probability density that there is immediately after the barrier, at the end of crossing, and this leads to estimate a dependence from $exp\left(-\frac{I_p}{E}\right)$, where $\frac{I_p}{E}$ is closely connected to the width of the barrier (through γ). For these calculations the electric field isn't constant during the electron passage, but it have a rising edge.

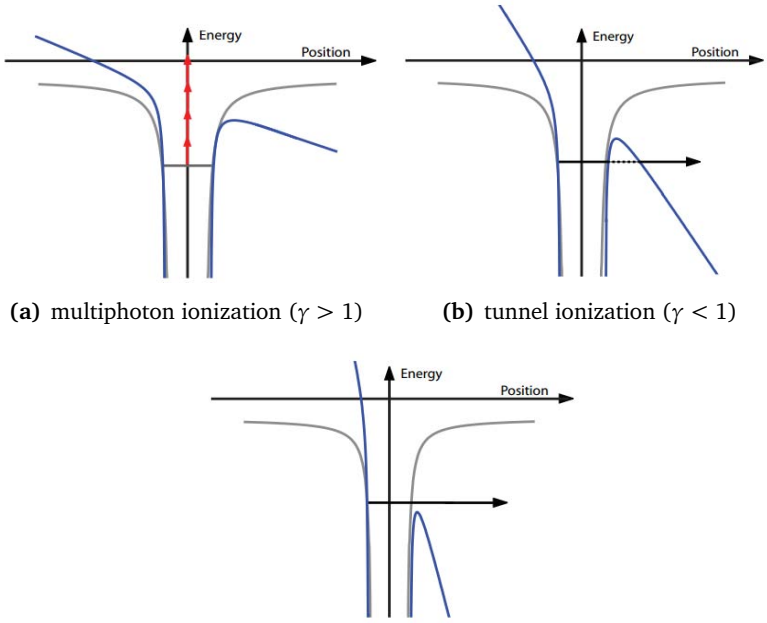

(a) multiphoton ionization ($\gamma > 1$) **(b)** tunnel ionization ($\gamma < 1$)

(c) above-barrier ionization ($\gamma << 1$)

Figure 2.3: Plots of the Coulomb potential (dotted line) and Coulomb potential modified by the laser field (solid line).

The Coulomb barrier may be suppressed below the ionization potential while there still exists a large population in the ground state (Fig. 2.3(c)). This is called above-barrier ionization and occurs for field strengths

in excess of the critical field strength:

$$E_{critical} = \frac{\pi \epsilon_0 I_p^2}{Ze^3} \tag{2.6}$$

where Z is the charge after ionization.
In this case, we can still use the adiabatic approximation, and so the ADK model, to calculate the ionization rate by averaging it over an optical period of laser.

2.1.2 Propagation

Once the electron is ionized, it passes from a condition in which it could occupy only a certain quantized energy state to one in which it can assume a continuum of energies, as if it was free. The condition in which electron can take every energy value with continuity is called continuum. In the continuum the electron can be treated classically and we can apply the classical mechanics to describe the electron motion and find its trajectories. Its motion can be thought as that of a charge in oscillating electric field.
We consider electron subjected only to the force produced by the incident laser electric field; in fact in the Lorentz force the magnetic field is weighted by v/c hence this contribution become important only for relativistic electrons.
It is worth mentioning that, in the strong-field approximation, the Coulomb field of the ion can be neglected with respect to the laser field.
So we consider an electric field of the form:

$$E(t) = E_0 cos(\omega_0 t) \tag{2.7}$$

We choose a reference system where electric field has one component in a specific direction, supposed the x-direction. The electron is accelerated in the direction of the electric field oscillation.
The Newton equation for the motion of a charge in electric field can be written as:

$$\ddot{x}(t) = \frac{q}{m_q} E_0 cos(\omega_0 t) \tag{2.8}$$

where q=-e is the charge and mq its mass. We call ti the ionization instant and t_r the recombination instant. Integrating the Eq. (2.10) using the initial condition $(t_i) = 0$, x$(t_i) = 0$, we obtain:

$$\dot{x}(t) = \frac{qE_0}{m_{q\omega_0}} (sin(\omega_0 t) - sin(\omega_0 t_i)) \tag{2.9}$$

and we finally obtain:

$$x(t) = \frac{eE_0 m_e}{\omega_0^2} (cos(\omega_0 t) - cos(\omega_0 t_i) + sin(\omega_0 t_i)(t - t_i)\omega_0) \tag{2.10}$$

At different ionization instants t_i correspond different trajectories which depend also on laser frequency and electric field amplitude (it's only a scale factor).

2.1.3 Recombination

The electron oscillating with the electric field has a certain probability to collide with the parent ion in a specific time. The more it rests in the continuum, the more its wave function broads, the more the superposition with the wave function of the bound state decreases and lower is the probability to collide with the ion.
We can find the instant t $= t_r$ in which the electron recombine with his parent ion solving the equation:

$$cos(\omega_0 t) - cos(\omega_0 t_i) + sin(\omega_0 t_i)(t - t_i)\omega_0 = 0 \tag{2.11}$$

All couples (t_i, t_r) solutions of this equation individuates a specific trajectory of the electron.

The Eq. (2.11) is a transcendental equation that can be solved graphically or numerically. When $\omega_0 t_i = 0° + k\pi, k \in N$ the electron recombines infinite times, but with zero velocity and so zero energy. The recombination is possible only for linearly polarized pulses.
For the conservation of energy the recombination of electron is followed by the radiation emission that can be seen as a photon emission when

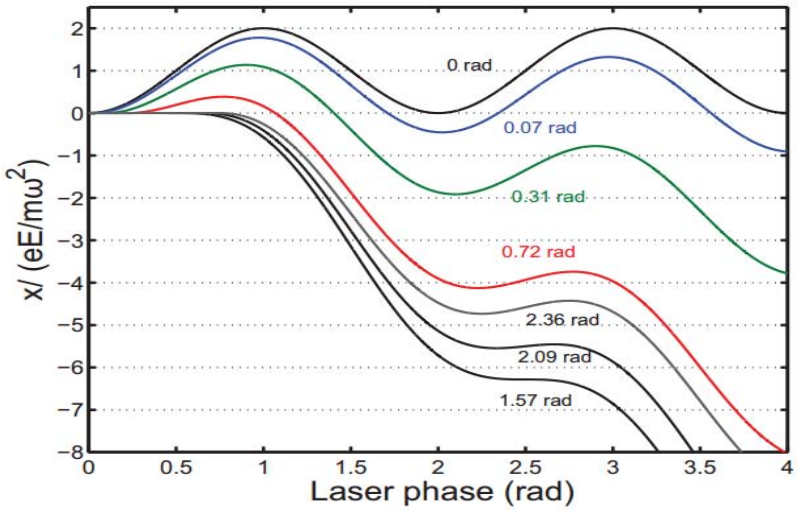

Figure 2.4: Possible paths for the electron during rescattering as a function of laser phase, and several selected values of the phase of the laser at ionization. Intersection with the x-axis indicates the possibility of recombination.

electron returns in its fundamental state:

$$E_{hhg} = I_p + K = I_p + \frac{1}{2} m_e \dot{x}^2 \tag{2.12}$$

Putting the Eq. (2.9) into the Eq. (2.11):

$$E_{hhg} = \hbar\omega_{hhg} = I_p + 2U_p[sin(\omega_0 t_r) - sin(\omega_0 t_i)]^2 \tag{2.13}$$

The maximum energy achieved by electron in the continuum is obtained for $\omega_0 t_i = 0.09\pi + k\pi$, $k \in N$ and $\omega_0 t_r = 1.4\pi + k\pi$, $k \in N$:

$$E_{hhg,MAX} = \hbar\omega_{cut} = I_p + 3.17U_p \tag{2.14}$$

$$\omega_{cut} = \frac{Ip + 3.17Up}{\hbar} \tag{2.15}$$

The (2.15) is defined as energy cut-off.
The spectrum irradiated for Bremsstrahlung, due to the sharp deceleration of the electron, is continuous and it's characterized by a plateau

followed by a cut-off.
The absence of even harmonics can be understood thinking to the medium non linear susceptibility, due to the anharmonicity introduced by electron recollisions.
If we consider a pulse of finite duration the harmonic line width is proportional to the inverse of the pulse duration. The more the pulse is short the more the spectrum is similar to a continuum.
The limit is a pulse with one optical cycle for which the spectrum is continuous. The presence of pulsed radiation causes that:

a) the number of optical cycles is finite and so the spectrum is characterized by broader peaks for shorter driving pulses;

b) the peaks in the cutoff region of the XUV spectrum are found to be shifted with respect to the expected harmonic frequencies owing to the phase shift between spectra emitted from consecutive recollision events, which occur at different laser intensities. [12]

This three-step process will repeat itself for every half cycle ($\lambda/2$) of the driving field, therefore generating odd harmonics of the driving field. This is due to symmetry considerations in the nonlinear optical process in fact the generation of even harmonics requires a medium without inversion symmetry, which does not exist in a gas.
If the symmetry is broken by introducing a second pulse of a different wavelength, it is possible to generate even and odd harmonics of the driving field.

Chapter 3

Optical elements characterization

3.1 Monochromator time broadening

The monochromator demanded for the spectral selection of ultrashort pulses has to preserve the temporal duration as short as in the generation process (32 fs by the project requirements).
A modest time broadening can be tolerated if the pulse duration at the output of the monochromator is anyway shorter than the temporal resolution required by the experiment.
The monochromator can be modeled as a filter with a complex frequency response that includes both the nonuniform spectral transmission and the distortion in the spectral phase. [13] Because the XUV pulse at the generation may be produced to be close to its transform limit, any modification of its complex spectrum results in a time broadening as described by its Fourier transform. For a Gaussian profile with no modulation of either phase or frequency, the duration at half-height $\Delta\tau$ has a lower limit expressed by the relation:

$$\Delta\tau = \frac{2ln(2)}{\pi c}\frac{\lambda^2}{\Delta\lambda} = \frac{0.44}{c}\frac{\lambda^2}{\Delta\lambda} \tag{3.1}$$

where λ is the pulse central wavelength, $\Delta\lambda$ is the spectral width at half-height, and c is the speed of light in a vacuum.
In order to preserve the duration of the pulse at the output of the monochromator, the selected bandwidth has to be larger than the spectral width of

the pulse $\Delta\lambda$; moreover, the transfer function has to be almost constant within the bandwidth.
The first condition is verified if the monochromator selects the whole spectral band of the pulse, so no modifications in the Fourier spectrum are induced. The second condition is almost always verified if the monochromator is realized by the reflecting optics, because the reflectivity variations within the bandwidth $\Delta\lambda$ are usually negligible, so that the transfer function can be considered almost constant, although lower than unity.
The use of a single grating inside the monochromator inevitably gives a distortion of the temporal profile of the ultrashort pulse because of diffraction. In fact, each ray that is diffracted by two adjacent grooves is delayed by $m\lambda$, where m is the diffraction order and λ is the wavelength. The total difference in the optical paths of the diffracted beam from the source to the image is given by $|m|\lambda N$, where N is the number of the illuminated grooves. For example, let us consider a 200 grooves/mm grating illuminated by radiation at 30 nm over a surface of 20 mm. The number of grooves that is involved in diffraction is 4000, giving a total delay of 120 μm, i.e., 400 fs.
This effect is negligible in the picosecond or longer time scale, but it is dramatic in the case of a femtosecond pulse because it reduces both the time resolution capability and the intensity at the exit of the monochromator.
We want to analyze the single-grating configuration to identify the condition to have the minimum temporal broadening from a grating.
Once the achievable resolution $R = \lambda/\Delta\lambda$ at the output of the monochromator has been defined, the minimum number of grooves N_{min} that have to be involved in the diffraction to support such a resolution is given by the relation $|m|N_{min} = \lambda/\Delta\lambda$ [14]. The corresponding total variation of the optical paths at the grating output is $\Delta OP_{TOT} = |m|\lambda N_{min} = \lambda^2/\Delta\lambda$, and its half-width is calculated as $\Delta OP_{min} \approx \frac{1}{2}\frac{\lambda^2}{\Delta\lambda}$. It follows that the diffraction from a single grating gives a *lower limit* for the duration at half-width $\Delta\tau_{G,min}$ at the output of the monochromator for a pulse with bandwidth $\Delta\lambda$ that is calculated as:

$$\Delta\tau_{G,min} \approx \frac{1}{2c}\frac{\lambda^2}{\Delta\lambda} \tag{3.2}$$

This is close to the Fourier limit given by Eq. (3.1).
The single-grating design can be adopted for ultrashort pulses without altering in a significant way the pulse duration, provided that the product of the number of illuminated grooves times the diffracted order is equal to the actual resolution. So the pulse temporal half-width after the diffraction is:

$$\Delta\tau_G \approx \frac{1}{2c} m\lambda N \tag{3.3}$$

3.2 Monochromator geometries

Grazing-incidence diffraction gratings may be used in two different geometries: the **classical diffraction mount (CDM)** and the **off-plane mount (OPM)**. The latter differs from the classical one in that the incident and diffracted wave vectors are almost parallel to the grating grooves.

3.2.1 CDM and OPM configurations

The CDM and OPM layouts are shown in Fig. 3.1.
Let us define the incidence angle α and the diffraction angle β , respectively, as the angles between the direction of the input beam and the normal to the grating and the direction of the diffracted beam and the normal to the grating. Both α and β are taken with positive signs.
When the grating is used as a monochromator, the subtended angle K = $\alpha + \beta$ is constant and the grating equation is normally expressed as [see App. D - Eq. (D.20)]:

$$\alpha = \frac{K}{2} + arcsin\left[\frac{m\lambda\sigma_{cd}}{2cos\,(K/2)}\right] \tag{3.4}$$

The number of illuminated grooves is N = $S\sigma_{cd}/cos\alpha$, where S is the beam section measured on the grating center in the direction normal to the light propagation. The illuminated area on the grating is smaller if the latter is used at order m = -1. This is the normal choice to maintain the number of illuminated grooves as small as possible.

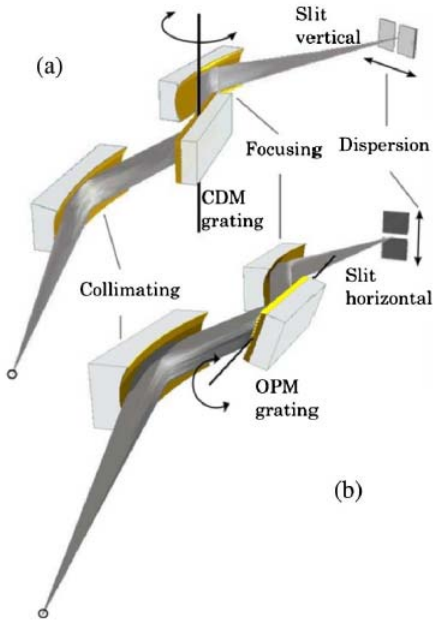

Figure 3.1: Layout of a plane-grating monochromator in (a) CDM and (b) OPM geometry.

The geometry and blaze condition for which the diffraction efficiency is maximized are illustrated for the CDM in Fig. 3.2.

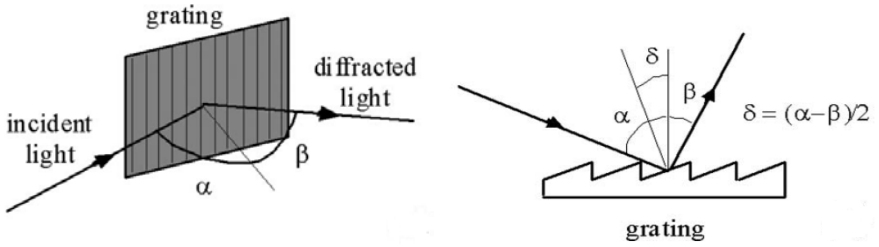

(a) Geometry of the CDM. **(b)** Blaze condition of maximum efficiency.

Figure 3.2: CDM mount.

The condition is fulfilled when the diffracted light leaves the grating in such a way to perform a specular reflection on the groove surface, i.e., when $\delta = (\alpha - \beta)/2$, where δ is the blaze angle of the grating.
In this case, the incident and diffracted wave vectors are almost parallel

to the grating grooves [15]. The direction of the incoming rays is described by two parameters: the altitude and the azimuth. The altitude γ is defined as the angle between the direction of the incoming rays and the direction of the grooves.
The azimuth μ of the incoming rays is defined to be zero if they lie in the plane perpendicular to the grating surface and parallel to the rulings. Let ν define the azimuth of the diffracted light at wavelength λ and order m.
The grating equation for the OPM is $sin\gamma(sin\mu + sin\nu) = m\lambda\sigma_{op}$, where σ_{op} is the groove density.
When used as a monochromator, the grating is operated in the condition $\mu = \nu$ and the grating equation is:

$$\mu = arcsin\left[\frac{m\lambda\sigma_{op}}{2sin\gamma}\right] \tag{3.5}$$

The number of illuminated grooves is $N_{op} = S\sigma_{op} = cos\mu$. The grating can be used indifferently at the orders m = ±1 because it does not affect the size of the optics.
The geometry and blaze condition for which the diffraction efficiency is maximized are illustrated for the OPM in Fig. 3.3.

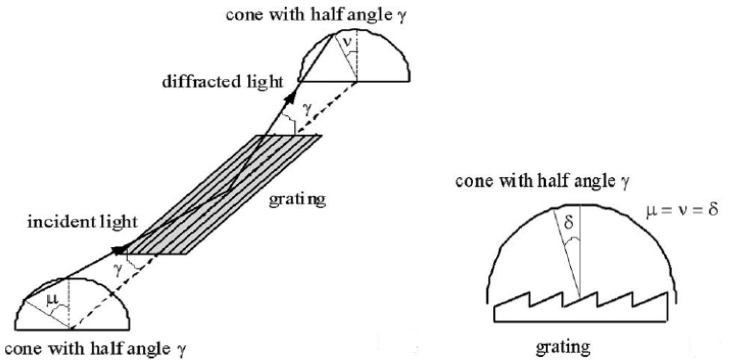

(a) Geometry of the OPM.

(b) Blaze condition of maximum efficiency.

Figure 3.3: OPM mount.

For the maximum diffraction efficiency the light has to leave the grating in such a way that it performs a specular reflection on the groove surface, that is $\delta_{op} = \mu = \nu$, where δ_{op} is the blaze angle of the grating.
The OPM gives higher throughput than the classical mount, because it has been theoretically demonstrated [16] and experimentally measured [17, 18] that the peak diffraction efficiency is close to the reflectivity of the coating at the altitude angle.
The OPM geometry is then a good candidate for the design of XUV monochromators with high efficiency.
Schematics of the two configurations with plane gratings operated in parallel light are shown in Fig. 3.4.

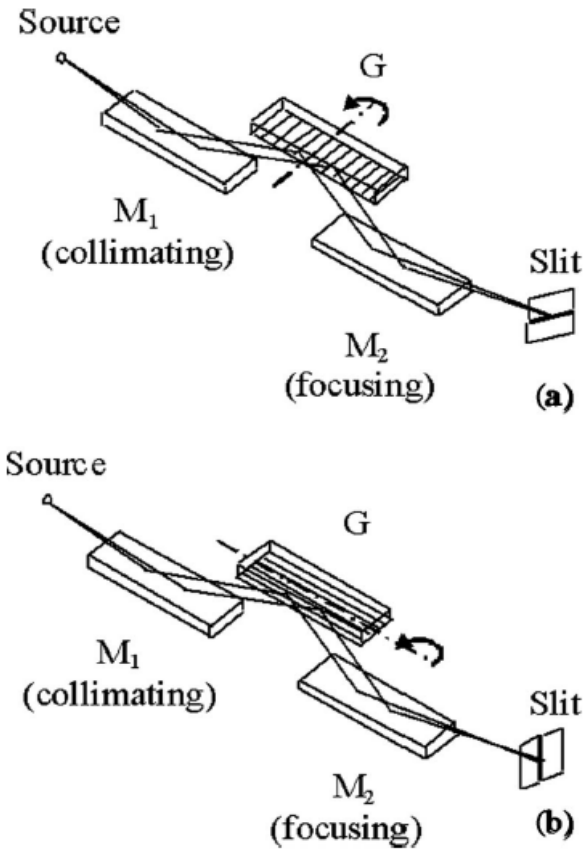

Figure 3.4: Schematics of the monochromator configuration with plane gratings: (a) CDM and (b) OPM.

A spectrally dispersed image of the source is created on the exit plane, where the slit carries out the spectral selection. The three optical elements are indicated as M1, G, and M2, where the letters M and G indicate, respectively, the mirrors and grating.
The first mirror (M_1) acts as the collimator; the second mirror (M_2) acts as the condenser. The two mirrors are operated at an equal grazing angle and unity magnification to minimize the aberrations, i.e., the length input arm of the collimator, p, i.e., the distance between the entrance source and the center of M_1, is equal to the output arm of the condenser, q, i.e., the distance between the center of M_2 and the exit slit: they are both equal to 600 mm in this project to reduce the risk of damaging or contaminating the optics with some debris that could propagate from the gas cell when the intense laser is focused on it. In the case of using toroidal optics, it has been shown that the best optical performances are obtained in the case of equal mirrors, because this minimizes the coma aberration (App. B). [19]
Let us suppose that the exit slit width, ΔS, is equal to or wider than the size of the XUV source at the input of the monochromator.
The monochromator can be operated either with or without an entrance slit. The latter is the normal case for analysis and utilization of HHs [20]. The number of illuminated grooves in the two geometries is indicated, respectively, as $N_{cd} = 2p\sigma_{cd}/cos\alpha$ and $N_{op} = 2p\sigma_{op}/cos\mu$ (S = 2p, where p is the half-width beam divergence at the input). The wavelength selection is performed by rotating the grating around an axis that is tangent to the surface, passes through the grating center, and is parallel to the grooves.
The half-width output bandwidth is:

$$\Delta\lambda_{cd} = \frac{cos\beta}{\sigma_{cd}}\frac{\Delta S}{mq} = \frac{cos(K-\alpha)}{\sigma}\frac{\Delta S}{mq} \tag{3.6}$$

$$\Delta\lambda_{op} = \frac{cos\mu}{\sigma_{op}}\frac{\Delta S}{mq} \approx \frac{1}{\sigma_{op}}\frac{\Delta S}{mq} \tag{3.7}$$

where $\Delta\lambda_{cd}$ refers to the CDM and $\Delta\lambda_{op}$ to the OPM, and the width of the exit slit is supposed to be the same in both cases. The approximation

in Eq. (3.7) is assumed for low-resolution designs when $\mu \leq 10°$, because $\cos \mu \simeq 1$.

3.2.2 CDM and OPM pulse width after diffraction

From Eq. (3.3) the pulse temporal half-width after the diffraction is $\Delta\tau_G \simeq \frac{1}{2c} m\lambda N$, that is:

$$\Delta\tau_{G,cd} = m\lambda p \frac{\sigma_{cd}}{cos\alpha}, \tag{3.8}$$

for the CDM and

$$\Delta\tau_{G,op} = m\lambda p \frac{\sigma_{op}}{cos\mu} \approx m\lambda p \sigma_{op}; \tag{3.9}$$

for the OPM, where the approximation $cos\mu \simeq 1$ is assumed in case of low-resolution configurations.
For a given beam section, the two configurations have the same temporal response if $\frac{\sigma_{cd}}{cos\alpha} = \frac{\sigma_{op}}{cos\mu} \simeq \sigma_{op}$. Therefore, the groove density to be used is to have the same resolution, and the same temporal response is lower in the CDM than in the OPM, $\sigma_{cd} < \sigma_{op}$, because α is in the range of $\approx 75° - 85°$ for grazing-incidence configurations and μ is typically lower than 10°.
The condition to preserve the temporal duration of the pulse with half-width duration $\Delta\tau$ after the diffraction from N grooves is finally

$$m\lambda p \frac{\sigma_{cd}}{cos\alpha} \leq c\Delta\tau, \tag{3.10}$$

for the CDM and

$$m\lambda p \frac{\sigma_{op}}{cos\mu} \approx m\lambda p \sigma_{op} \leq c\Delta\tau; \tag{3.11}$$

for the OPM. If the conditions stated by equations (3.10) and (3.11) are satisfied, the monochromator called to make the spectral selection is defined to be **time preserving**, *because the pulse duration at the output is preserved*.
The shorter the pulse whose duration has to be preserved after the monochromatization, the lower the requested spectral resolution.

3.2.3 CDM and OPM main advantages and drawbacks

The main advantage of the OPM when compared with the CDM is the higher diffraction efficiency, which has been measured to be actually close to the coating reflectivity at the same altitude [21, 22]; on the other hand, the main drawback is the distortion and the rotation of the image after the diffraction, which is due to the highly nonspecular reflection from the grating, especially for the large azimuth angles, which are required to achieve high spectral resolution (see App. D). [23]
This makes the OPM much more complex to be adopted than the CDM for high resolution designs. Indeed, for low-resolution designs, as those required for ultrafast pulses, the distortion and rotation are almost negligible, since the azimuth angle is low.
Assumeing that the grating is operated in the first diffracted order, as is typical in most cases and the half-width beam section on the grating is assumed to be 1 mm. We analyze two different temporal regimes: 100 or 20 fs half-width pulse front tilt at 30 nm (41 eV). The corresponding maximum number of illuminated grooves to support such a time response is 2000 for 100 fs and 400 for 20 fs.
Observing Fig. 3.5 CDM and OPM are compared at two wavelengths in terms of grating characteristics for front tilts in the 10-200 fs range.
In the case of the CDM, as the subtended angle increases, the corresponding groove density decreases. In the case of the OPM, the groove density is almost independent from the choice of the altitude angle.
The blaze angle that maximizes the grating efficiency in the CDM is definitely lower than that in the OPM.
In addiction CDM monochromators with front tilts in the range of hundreds of femtoseconds require the use of gratings with blaze angles around 1°, which are well within the present capabilities of manufacturers.
Instead, front tilts in the range of a few tens of femtoseconds require an extremely low groove density in the CDM and a blaze angle that is practically unfeasible, so that laminar profiles have to be adopted with extremely low efficiency. In contrast, the blaze angles required in the OPM configurations are less extreme than in the CDM.

For front tilts below 100 fs, the blaze angles required for gratings in the CDM are beyond the present capabilities of manufacturers, while the CDM requires groove densities and blaze angles that are feasible and give high efficiency. For front tilts longer than 100 fs, the OPM requires high azimuth angles especially for short wavelengths; this is not a suitable configuration, since it introduces a large anamorphic deformation. As a general claim, the CDM should be preferred for monochromators when relatively large front tilts, i.e., 100–200 fs, are accepted and medium-high spectral resolution is required, while the OPM has to be adopted for ultrafast responses in the 10–50 fs range and low spectral resolution.

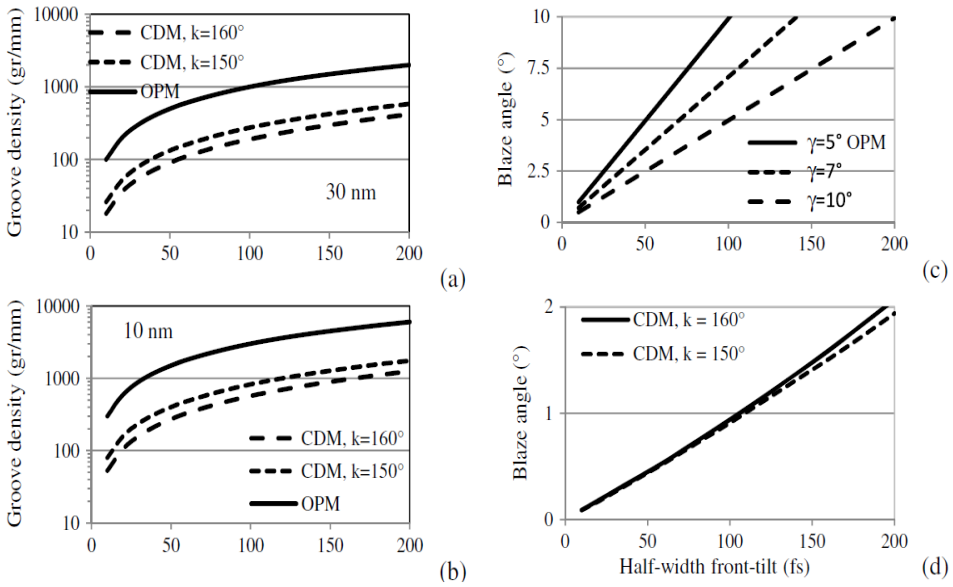

Figure 3.5: Ultrafast monochromator in CDM and OPM for 1 mm half-width beam section on the grating. (a) and (b) Groove density as a function of the pulse front tilt at (a) 30 nm and (b) 10 nm. (c) Corresponding blaze angle for the OPM at three altitudes. (d) Corresponding blaze angle for the CDM at two subtended angles.

Chapter 4

Experimental setup

This chapter aims to present the laboratory setup and the instruments used to carry out the experiments in this thesis work.
The first section will provide a description of the XUV sources that are usually adopted for the generation of the XUV beamline in absence of a source for HHg generation. They are the hollow-cathode XUV lamp and the Manson X-ray source. Then we will describe the apparatus used to perform experiments in vacuum, in order to avoid the strong absorbtion of XUV and soft X-ray radiation in air. Finally we will describe the alignment activity, and we will present the characterization of the instrument in the XUV and in the soft-X-ray regimes.

4.1 Sources

There are many processes that lead to an emission in the soft X-ray or XUV region, and they have an involved energy, release by a radiative process, of about $10^2 - 10^4$ eV. There are two types of emission processes:

- **Natural processes almost always happen by spontaneous emission with an isotropic and not synchronized emission.**

- Stimulated processes, where the emission isn't isotropic but directed and time-synchronized.

Considering natural processes, we can't realize a spontaneous emission source by heating because of the very high temperature required for the energies emission of thousands of eV. Considering that, for example the average kinetics energy of a gas mulecules is $E_k = \frac{3}{2}KT$, with K $= 8.6 \cdot 10^{-5}$ eV/$°K$ is the Boltzmann constant; in order to have an energy of 1 keV we need a temperature of $\simeq 8 \cdot 10^6$ $°K$. Emission by heating, instead, is possible for the visible light, as demonstrated by black body experiment. Therefore, spontaneous emission is realized in two ways:

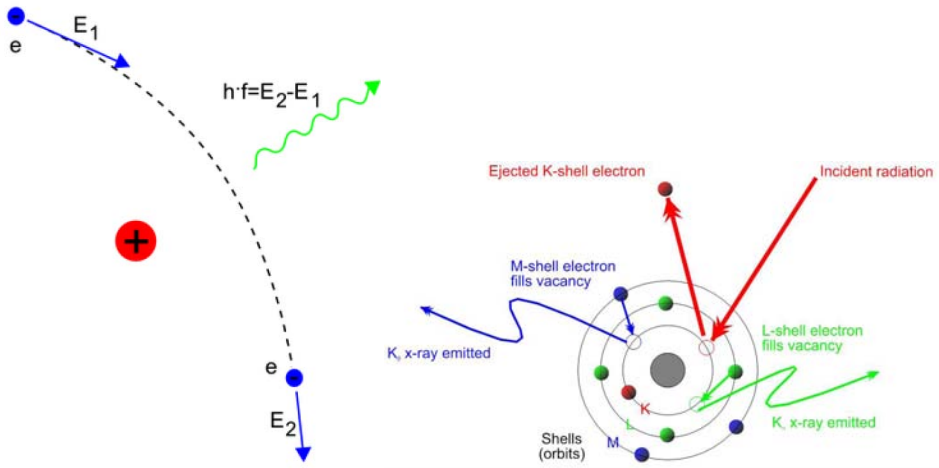

(a) Bremmstrahlung. **(b)** Fluorescence X.

Figure 4.1: a)Bremmstrahlung radiation; b)X-Fluorescence radiation representations.

- **Bremsstrahlung:** From classic physics theory a charge particle (electron) submitted to a negative acceleration, caused by impacting a metal material, looses energy, which can be emitted in a radiative form or by a crystalline lattice vibration (impact material heating). The energy lost will be $h\nu = \Delta E = E_{fin} - E_{in}$. This emission happens in a large interval of frequencies (Fig. 4.1(a)).

- **Fluorescence X:** From semi-classic Bohr atomic model electrons in an atom rotate in discrete orbits, without loosing energy. The only way to loose energy by an electron is the orbit transition. When a particle creates a hole, caused by impacting an electron in a par-

ticular shell of the atom, this one can be filled by an electron in an outer shell with the consequent emission of an energy with a specific wavelength equal to the energy gap between two shells. This process produces a **characteristic emission spectrum** of XUV and X-rays at a few discrete frequencies, sometimes referred to as the spectral lines. The spectral lines generated depend on the target (anode) element (Fig. 4.1(b)).

For sources that we will describe we have the combination of the previous two different emissions (Fig. 4.2). Furthermore a vacuum system is necessary in order to avoid the traveling particle (electron) immediate recombination in air.

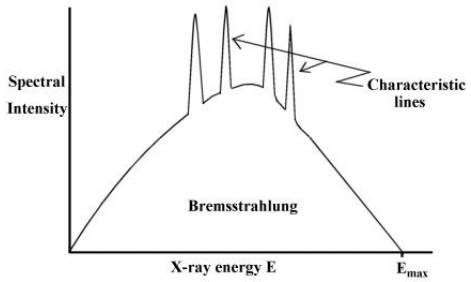

Figure 4.2: Combination of Bremmstrahlung and Fluorescence radiations spectrum.

4.1.1 The Microfocus Manson soft X-ray source

Manson X-ray Source (Fig. 4.3) was developed for use in the radiometric calibration of grazing incidence spectrometers, and its design features have made it useful in other applications as well. A special feature is that two equivalent output beams are provided, from two views of the single emitting spot (cathode) where the electron beam from the hairpin tungsten filament collides with the replaceable anode cap usually made of carbon, copper, silicon, alluminium and magnesium, see Fig. 4.4.
This spot is between 0.2 and 2 mm in diameter, depending on the voltage and current applied between anode and cathode. This geometry is intended to allow monitoring of one beam by an absolute photon counter

while the other beam is used to calibrate the instrument or provide a known flux for some other purpose.
These electrons impact on the anode's atoms exciting them; when they decay to lower states, they will emit Bremmstrahlung Fluorescence soft X-ray radiation.
This source is completely open in the atomic bombardment, so the entire source is in vacuum. The source emits in the **5-30 nm** region.
A power source is used to establish the currents and potentials needed to run the X-ray Manson source.

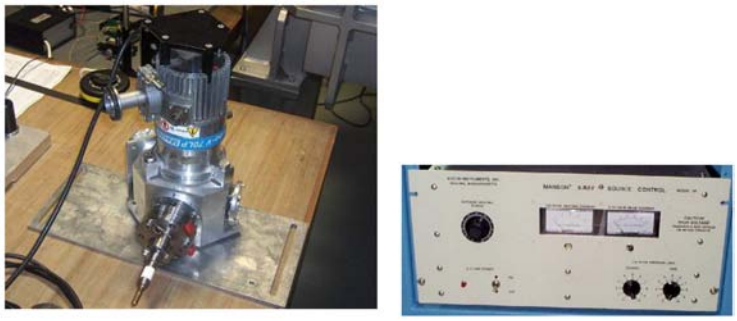

(a) Layout of the source. **(b)** Power source.

Figure 4.3: a)Layout of the source; b)Power source.

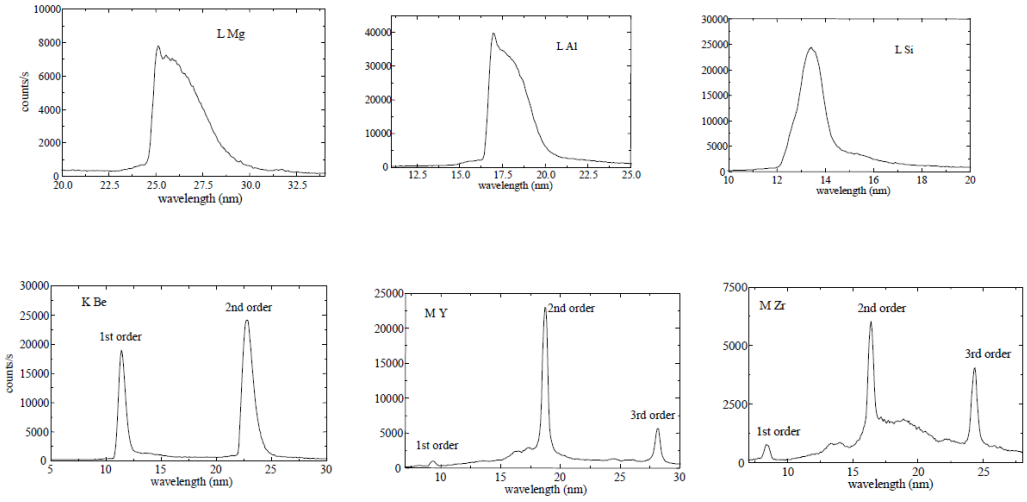

Figure 4.4: Manson source spectra obtained with different anode materials.

4.1.2 The hollow-cathode lamp

An Hollow-cathode lamp (Fig. 4.5 and 4.6) is made of a glass tube containing a cathode, an anode, and a buffer gas (usually a noble gas i.e. He, Ne).
A large voltage across the anode and cathode will cause the buffer gas to ionize, creating a plasma.
The buffer gas positive ions will then be accelerated into the cathode, sputtering off atoms from the cathode. Both the buffer gas and the sputtered cathode atoms will in turn be excited by collisions with other atoms/particles in the plasma.
As these excited atoms decay to lower states, they will emit photons, which can then be detected and a spectrum can be determined. Either the spectrum from the buffer gas or the sputtered cathode material itself, or both, may be of interest, see Fig. 4.7).

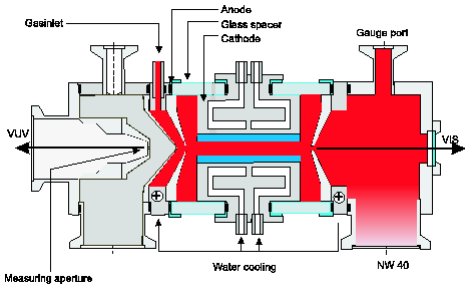

Figure 4.5: Schematics of a hollow-cathode lamp.

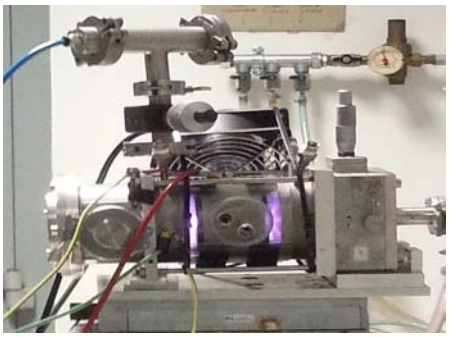

Figure 4.6: Hollow-cathode lamp used for the facility. The purple color of plasma stays for using helium gas as buffer.

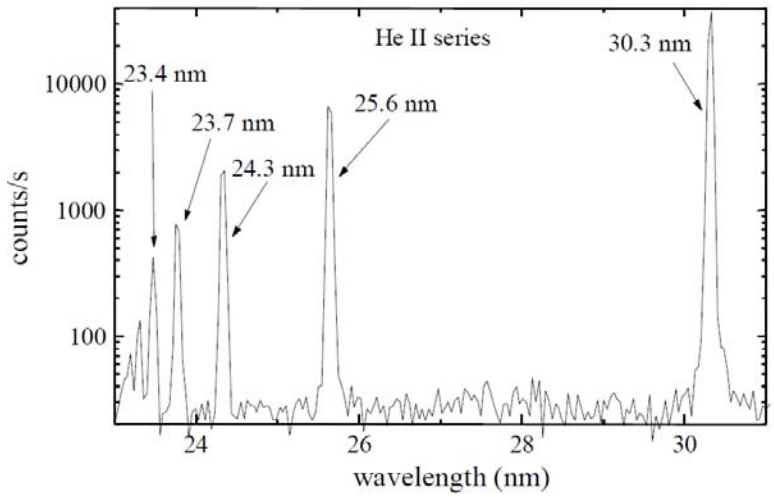

Figure 4.7: Spectrum emitted by an hollow-cathode lamp filled with helium. The range is 10-40 nm.

4.2 Monochromator design

A schematic view of the monochromator system is shown in Fig. 4.8. It consists of an entrance vertical slit; three interchangeable plane gratings between two toroidal mirrors in the first chamber, the exit vertical slit and a second photodiode chamber, from wich comes out the pico-current signal associated to the photon flux intensity, that can be measured by a Picoammeter and further analyzed by means of an acquisition system. The gratings are used in the **classical diffraction mount (CDM)**.

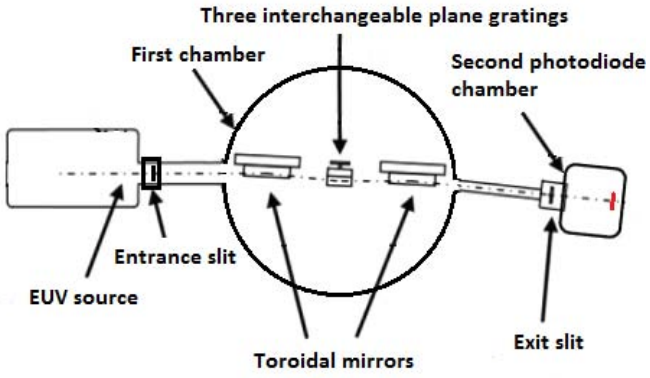

Figure 4.8: Schematic of the monochromator.

- **Vertical entrance slit:** Since we are working with tens of nm wavelengths, the predominant phenomenon to take into account are aberrations (see App. D), a slit can limit the beam aperture of hollow-cathode or Manson sources having negligible diffraction effects on the transmitted beam shape. However, the result of closing the slit is an incresing of central maximum beam diffraction width. Therefore even the spectra resolution increases, making it possible to distinguish nearby spectral lines emitted by the source with the drawback of having a decrease of beam intensity.

- **Two toroidal mirrors:** (see Fig. 4.9) This components allow the compensation of the astigmatism aberration [App. B] and produces a stigmatic beam by focusing the radiation also in the direction perpendicular to the grating dispersion plane (sagittal plane) [App. C].

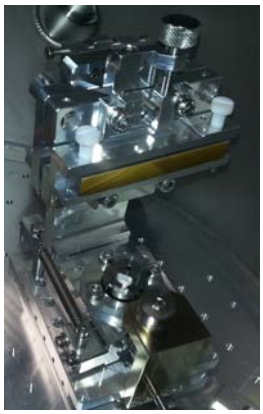

Figure 4.9: Toroidal gold coated mirror in the monochromator chamber.

The equations to consider are:

$$tangential\ \ plane \quad \frac{1}{p}+\frac{1}{q}=\frac{2}{Rcos\alpha} \tag{4.1}$$

$$sagittal\ \ plane \quad \frac{1}{p}+\frac{1}{q'}=\frac{2cos\alpha}{\rho} \tag{4.2}$$

Where R and ρ are, respectively the tangential and sagittal curvature radiuses, and α is the incidence angle respect to the normal of the mirror. Considering the first toroidal mirror, p (entrance arm) is the tangential and even sagittal distance between the entrance slit and first mirror, q and q' are the tangential and sagittal focuses (exit arms) towards the selected plane grating.
In our case, considering p = 600 mm; both q and q' equal to ∞, in order to have collimation; α is equal to 3°; the equations (4.1)-(4.2) become:

$$tangential\ \ plane \quad \frac{1}{p} = \frac{2}{Rcos\alpha} \Rightarrow R = \frac{2p}{cos\alpha} = 22900mm \quad (4.3)$$

$$sagittal\ \ plane \quad \frac{1}{p} = \frac{2cos\alpha}{\rho} \Rightarrow \rho = 2pcos\alpha = 62.80mm \quad (4.4)$$

For the second mirror (condenser) we have the same considerations, but in this case p = ∞ and both q and q' equal to 600 mm for the focusing (tangential and sagittal) of the collimated beam outgoing from the second toroidal mirror on the exit slit, having finally the same results.

- **Three motorized grazing incidence plane gratings:** (see Fig. 4.10) They allow to disperse the radiation spectral components (see App. D).

  In order to realize the selection and rotation of each one of three diffraction gratings with different groove densities σ, we used a motorized two axis motor: a slit supports the three gratings in sequence, which in turn can rotate on a support with a precision of 0.01°.

- **Exit vertical slit:** Its purpose (Fig. 4.11(a)) is blocking all the undesired radiation, having the selection of a single diffraction order of a wavelength present in the source polychromatic light. As for the entrance slit, the exit beam resolution can be increased by closing the slit, having, as counterpart a lower intensity.

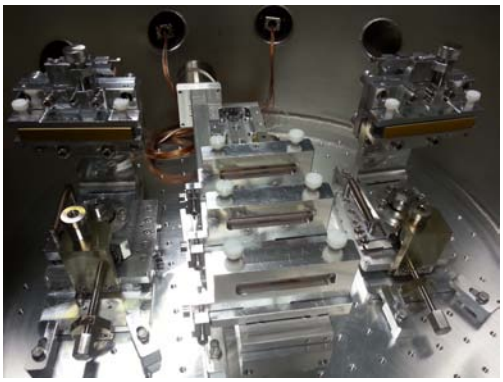

Figure 4.10: Two axis motor with the slit supporting each diffraction grating.

- **Photodiode, Picoammeter and remote control:** The detection of photon flux is performed by a photodiode in a second vacuum chamber (Fig. 4.11(b)), which rotate on its axis for the correct alignment with the beam. The picocurrent emitted by the p-n junction of the photodiode (powered with a 60 V voltage) is then measured by a picoammeter, which can perform a remote control with a PC (via GPIB connection) for consecutive (at $\approx$ ms intervals) current readings during a grating rotation.

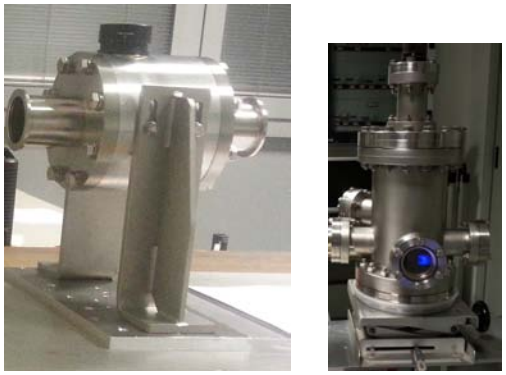

(a) Exit vertical slit. **(b)** Photodiode chamber.

Figure 4.11: The exit slit a) and the detector chamber b) of the monochromator system.

4.3 Gratings efficiency and output bandwidth

The efficiency of the different gratings employed in the monochromator (reported in Tab. 4) has been simulated computing the electromagnetic propagation and the grating efficiency. The simulated efficiencies of the gratings are reported in Fig. 4.12 for three different subtended angles.

Mirrors	Toroidal
Arms	600 mm
Grazing angle	3°
Radii	22900 mm × 62.8 mm
Coating	Gold
Coated area	60 mm × 10 mm
Maximum acceptance angle	5 mrad × 5 mrad
Gratings	3 plane grating
Constant subtended angle	160° (tentative)
Coating	Gold
Ruled area	40 mm × 10 mm
Grating #1	
Spectral region	30-90 eV
Groove density	600 gr/mm
Blaze angle	2°
Grating #2	
Spectral region	25-45 eV
Groove density	246 gr/mm
Blaze angle	1.6°
Grating #3	
Spectral region	15-30 eV
Groove density	150 gr/mm
Blaze angle	1.2°
Exit slit	
Width	> 50 μm, manual actuator Normally kept at 100 μm
Height	2 mm

Tab. 4 Main features of the three gratings.

The simulated output bandwidth, calculated as the FWHM bandwidth on a 100-um exit slit, and the pulse front-tilt, calculated as the FWHM front-tilt with a 3 mrad beam divergence, are shown in Fig. 4.13.
The FWHM beam divergence has been assumed to be 1.5 mrad, according to what has been measured on the CITIUS beamline in Nova Gorica (Slovenia), that is using similar laser parameters to generate HHs.
As a matter of comparison, three different subtended angles have been supposed, $150° - 155° - 160°$. The lower angle gives wider bandwidth and shorter front-tilt, on the contrary the higher angle gives narrower bandwidth and longer front-tilt.
Clearly, the front-tilt depends on the horizontal accepted aperture because this changes the illuminated area on the grating.
A limitator that is manually actuated may be placed just in front of the first toroidal mirror to limit the beam aperture. To achieve the temporal response shown in Fig. 4.13, the XUV beam horizontal aperture in front of the first toroidal mirror has to be limited to 1.8 mm. If the beam is limited to 1.5-mrad full aperture, i.e. 0.9-mm slit aperture, the front-tilt is reduced by a factor two.

The choice of the actual subtended angle has to take into account the spectral region of operation of the three gratings. It is recommended a choice of $\approx 160°$, that gives a rather high efficiency for all the gratings in the whole operational interval.

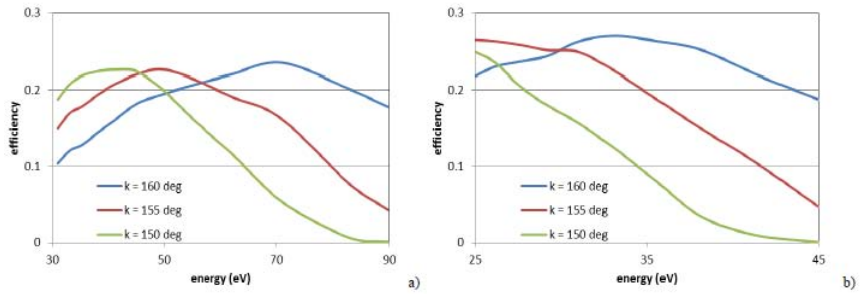

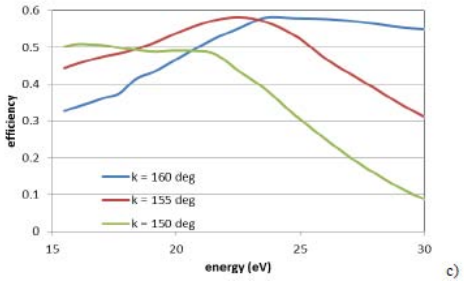

Figure 4.12: Grating efficiencies for three different subtended angles: a) 600 gr/mm grating; b) 246 gr/mm grating; c) 150 gr/mm grating, for K = 150°-155°-160°.

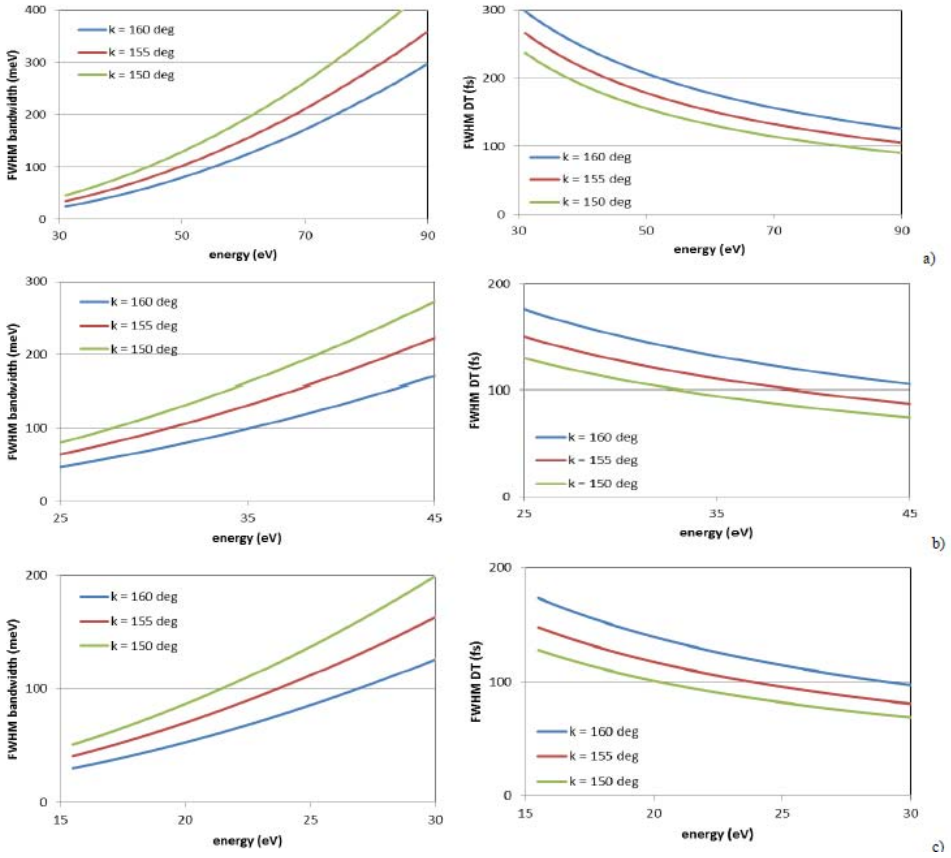

Figure 4.13: Simulations of FWHM bandwidth on 100-um slit, 50-um XUV source size and FWHM pulse front-tilt with 3-mrad full divergence: a) 600 gr/mm grating; b) 246 gr/mm grating; c) 150 gr/mm grating, for K = 150°-155°-160°.

4.4 Optical allignment

The optical allignment is accomplished using a low-intensity visible red laser (He-Ne with $\lambda = 630$ nm) to perform a correct disposal of all optics inside the monochromator.
The optical design of the alignment and the project design of the monochromator are represented in Fig. 4.14(a) and 4.14(b).

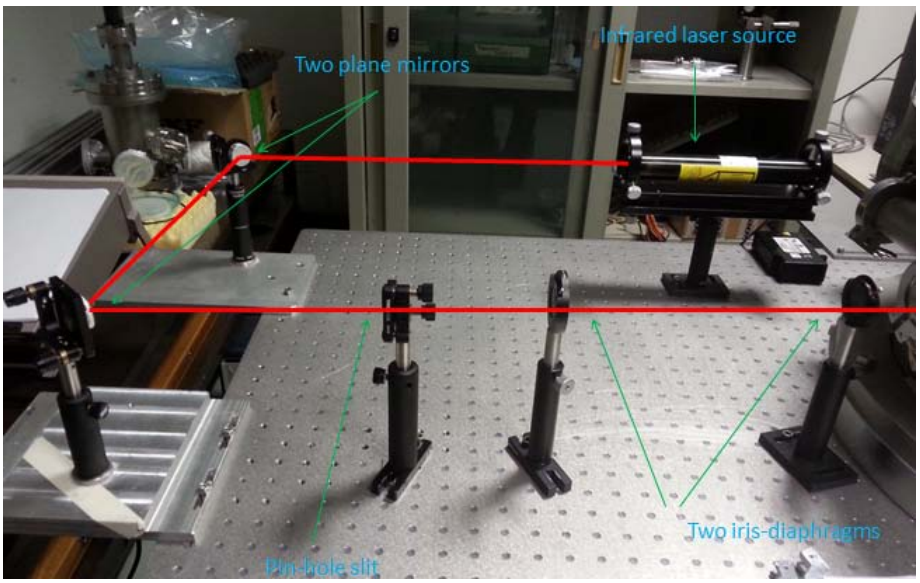

(a) Top-view of the optical design adopted for the alignment of the monochromator.

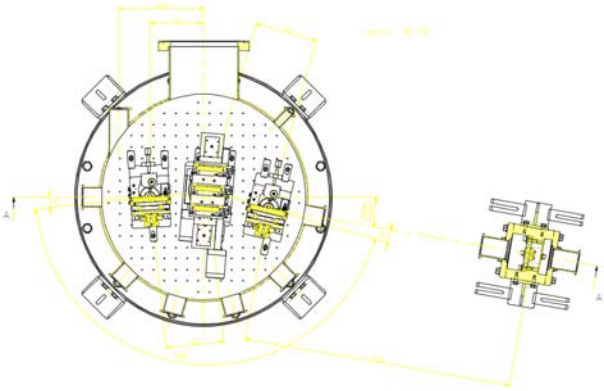

(b) Project design of the monochromator.

Figure 4.14: Optical alignment.

We realized the optical path of the laser beam by means of two plane mirrors in order to simulate source with an infinite distance from the pin-hole, with the purpose of having the propagation of plane wave-fronts (similar as much as possible to the real source beam) before the pin-hole slit, necessary to have a point-like source at 600 mm from the centre of the first toroidal mirror and two iris diaphragms to limit the effects of diffraction near the entrance of the monochromator. In a second moment, when the source (i.e. the hollow-cathode one) will be mounted, a vertical slit will replace the pin-hole, to limit the beam only in the tangential plane.
The next step is having an accurate precision adjustments about rotation and position of the optics, with the centering of the laser beam in the middle of the two toroidal mirrors and gratings (Fig. 4.15 and 4.16).

Figure 4.15: Beam footprint on the center of the first toroidal mirror.

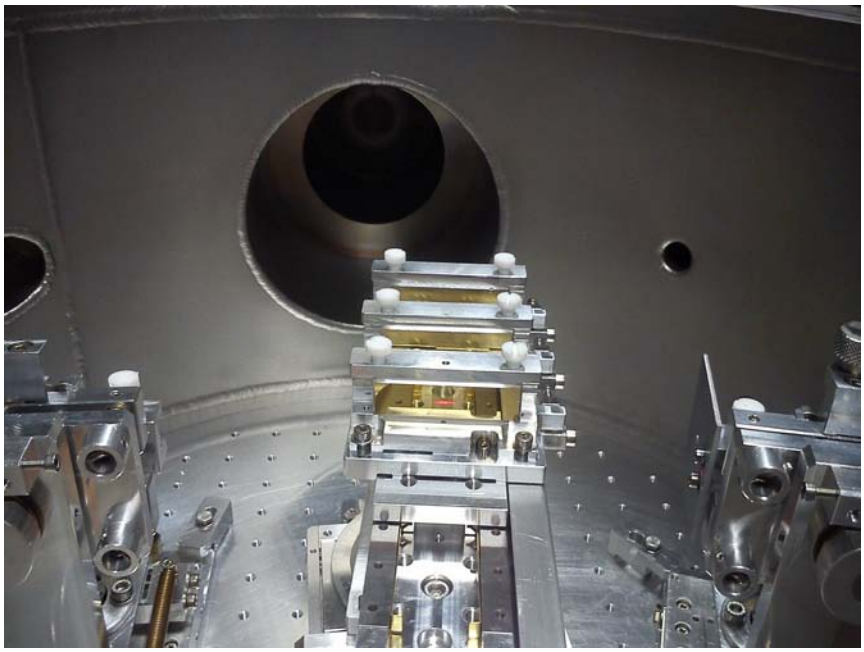

Figure 4.16: Beam footprint on the center of a plane grating.

We have choosen an anti-blaze (incidence angle $\alpha <$ diffraction angle β) arrangement of the three gratings to minimize the pulse-front tilt.
After the first toroidal mirror grazing incidence, the laser beam angle referred to the entry port of the monochromator must be deviated of about 6°, taking in account that the subtended angle K of the gratings is constant of about 158°.
Finally, the beam will be deviated again of 6° by a second toroidal mirror and will go through the exit port of the monochromator chamber.
At the end, we performed the verification of the exit spot profile through a beam-profiler; the acquisition is reported Fig. 4.17.
In each grating we have to check carefully the perpendicular incidence of the beam on the facet because a little up or down angle deviation leads to a conical diffraction.
The next step is the positioning of the vertical slit at the right distance of 600 mm from the second toroidal mirror to have the tangential focusing.
When the alignment phase has been finished, the source has been mounted immediately before the entrance slit (positioned in place of the pin-hole)

and all the system has been enclosed by vacuum tubes and bellows (Fig. 4.18).

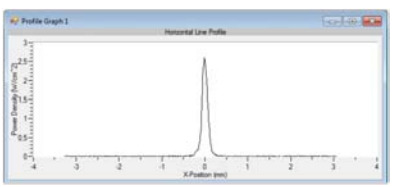

(a) Exit horizontal line profile.

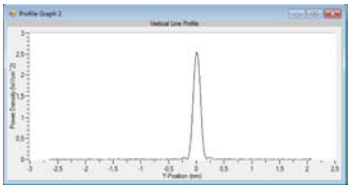

(b) Exit vertical line profile.

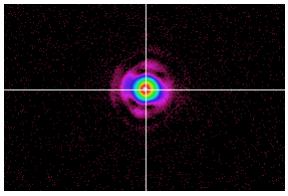

(c) Exit spot intensity after allignment phase.

Figure 4.17: BeamStar software analysis of the beam shape and intensity profile at the exit of the monochromator chamber.

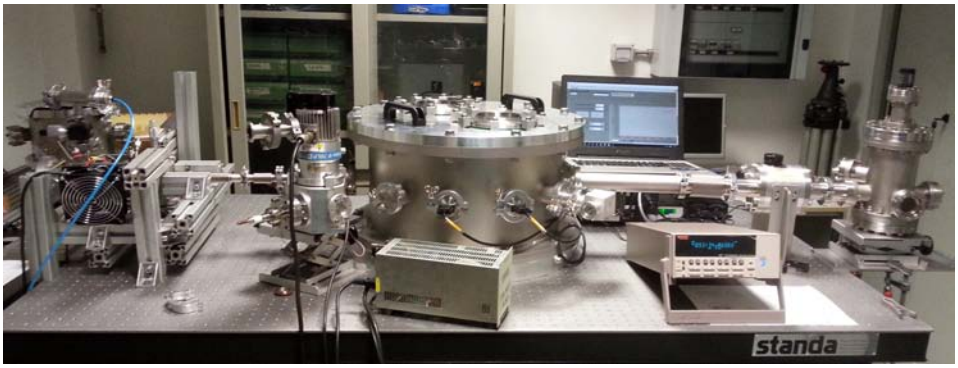

Figure 4.18: Final vacuum system composed by the hollow-cathod source, entrance slit, monochomator chamber, exit slit, and photodiode chamber.

4.5 XUV tests and characterization of the instrument

When the allignment has been finished, we dealt with the positioning of the entrance slit of the XUV source instead of the pin-hole, used in the visible (at 600 mm from the center of the entrance toroidal mirror). We had particular attention with the source setting in order to avoid misalignment in this spectral region.
The system has been sent in high-vacuum (with a pressure of 10^{-6} mbar) by means of a pump system correctly dimensioned.
Afterwards we had re-correct the three gratings position (traslation and rotation) in order to maximize the photons flux in reflection (0 order) collected by the photodiode.
Therefore, after several attempts we proceeded with making angular scannings of gratings by rotating them in prearranged intervals; this has been done with the use of Labview software by the for-cycle that I have implemented (see Ch. 5).
We have obtained the following spectra (Fig. 4.20, 4.21,4.22, 4.23, 4.24, 4.25) with an hollow-cathode source filled with He and Ne. In the tables 4.1, 4.2, 4.3 are reported the theoretical and measured values of gratings rotation (referred to 0 order) concerning a specific wavelength diffracted at the order -1 and the associated spectral lines current values (pA). The theoretical values of gratings rotation are in agreement with the measured values. This results has been obtained with entry and exit diaphgrams positioned immediately before and after, the entrance and exit toroidal mirrors (see Fig. 4.19) in order to avoid undesired reflections in the monochromator chamber.

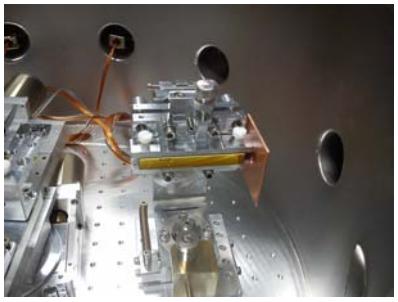

Figure 4.19: Diaphragm before the first toroidal mirror.

Table 4.1: Groove Density $\sigma = 150$ gr/mm

i.w. λ (nm)	Diffraction order	Th. Grating rotation (°)	Meas. Grating rotation (°)	Meas. current (pA)
	0	0	0	1.62
46 [Ne]	-1	-1.10	-1.00	1.10
74.4 [Ne]	-1	-1.68	-1.65	4.25
	0	0	0	1.50
30.4 [He]	-1	-0.69	-0.63	0.20
51.2-52.2 [He]	-1	-1.16	-1.10	0.35
58.4 [He]	-1	-1.32	-1.22	7.10

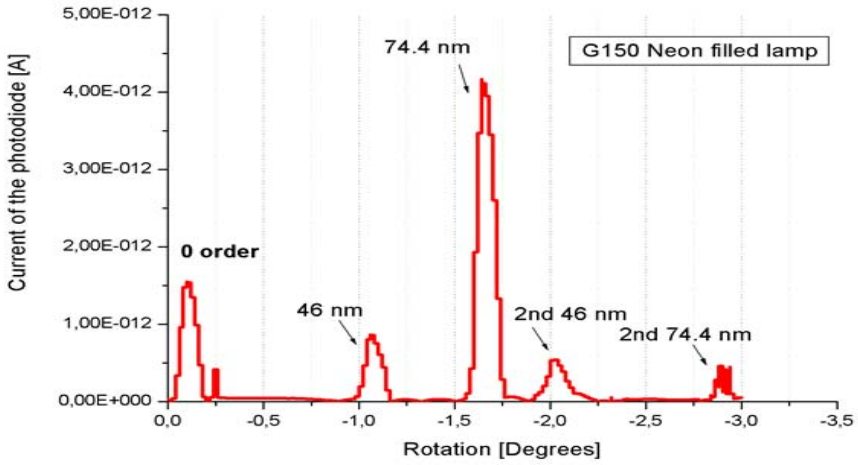

Figure 4.20: Ne measured current spectrum for the 150 gr/mm grating for negative diffraction orders.

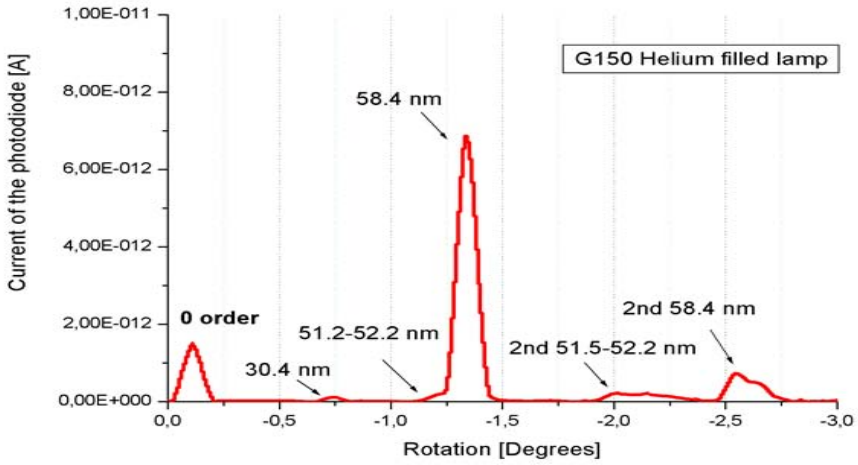

Figure 4.21: He measured current spectrum for the 150 gr/mm grating for negative diffraction orders.

Table 4.2: Groove Density $\sigma = 246$ gr/mm

i.w. λ (nm)	Diffraction order	Th. Grating rotation (°)	Meas. Grating rotation (°)	Meas. current (pA)
	0	0	0	12.40
35.3 [Ne]	-1	-1.31	-1.33	0.10
40.6 [Ne]	-1	-1.50	-1.40	0.17
46 [Ne]	-1	-1.70	-1.60	3.75
74.4 [Ne]	-1	-2.75	-2.70	6.23
	0	0	0	1.50
25.6 [He]	-1	-0.95	-0.95	0.05
30.4 [He]	-1	-1.13	-1.05	1.18
53.7 [He]	-1	-1.99	-1.85	0.78
58.4 [He]	-1	-2.16	-2.04	10.83

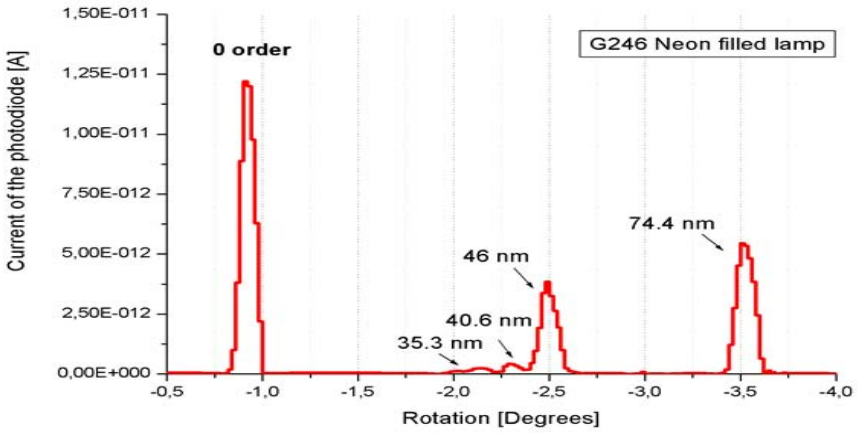

Figure 4.22: Ne measured current spectrum for the 246 gr/mm grating for negative diffraction orders.

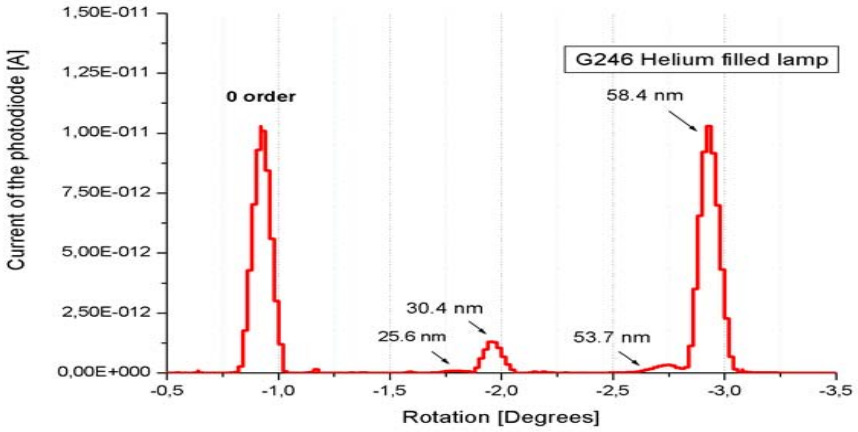

Figure 4.23: He measured current spectrum for the 246 gr/mm grating for negative diffraction orders.

Table 4.3: Groove Density $\sigma = 600$ gr/mm

i.w. λ (nm)	Diffraction order	Th. Grating rotation (°)	Meas. Grating rotation (°)	Meas. current (pA)
	0	0	0	3.82
46 [Ne]	-1	-4.15	-4.05	1.11
74.4 [Ne]	-1	-6.72	-6.24	0.55
	0	0	0	21.2
30.4 [He]	-1	-2.74	-2.52	1.22
58.4 [He]	-1	-5.27	-4.95	2.32

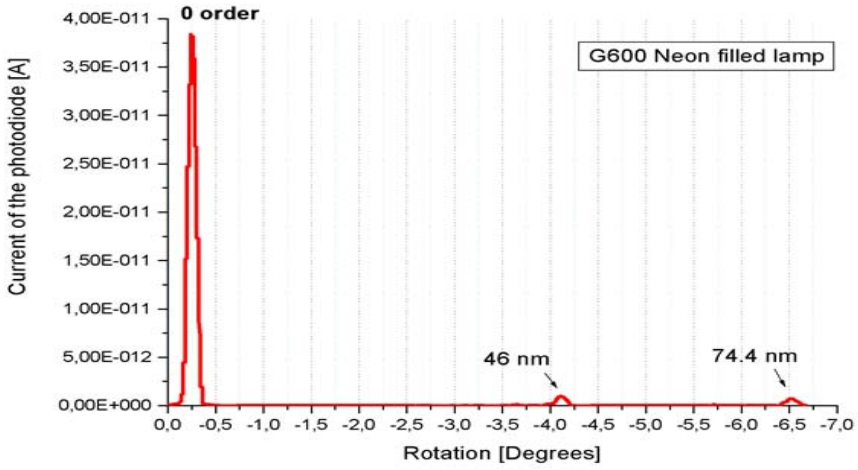

Figure 4.24: Ne measured current spectrum for the 600 gr/mm grating for negative diffraction orders.

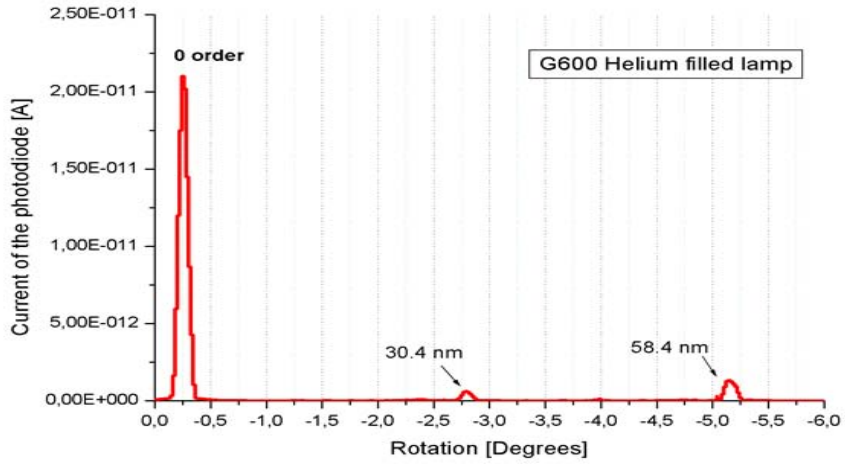

Figure 4.25: He measured current spectrum for the 600 gr/mm grating for negative diffraction orders.

4.6 Time response

In Fig. 4.26, 4.27 and 4.28 are reported the pulse temporal half-widths after diffraction for the three different gratings, in their spectral region; considering a 4 mrad beam aperture source.
The 600 gr/mm grating has a higher slope at wavelength increasing than 150 and 246 gr/mm gratings, and it's more susceptible to a time broadening of the pulse.

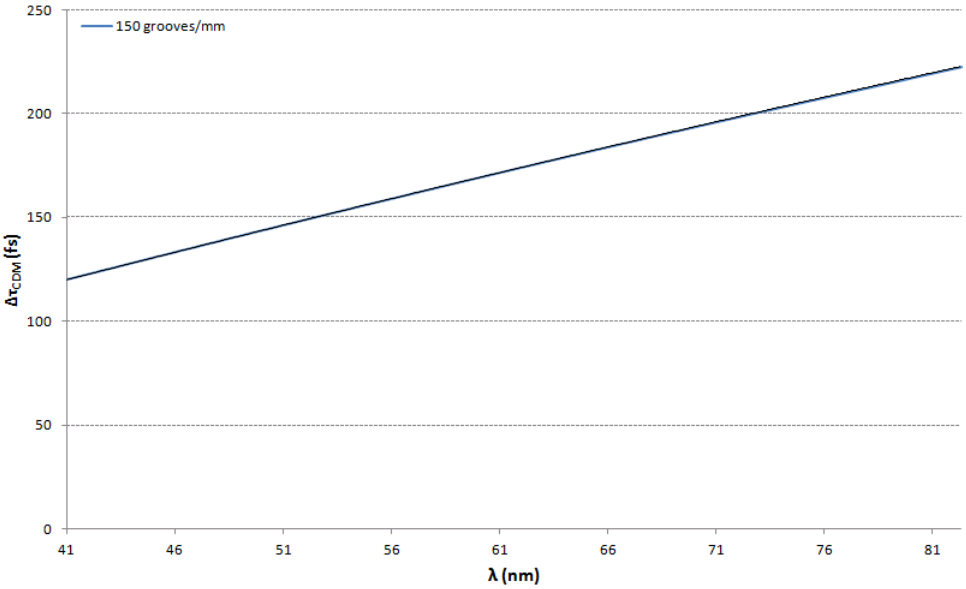

Figure 4.26: FWHM pulse front-tilt with 4-mrad full divergence, for 150 gr/mm grating, in the 15-30 eV (41.33-82.66 nm) spectral range.

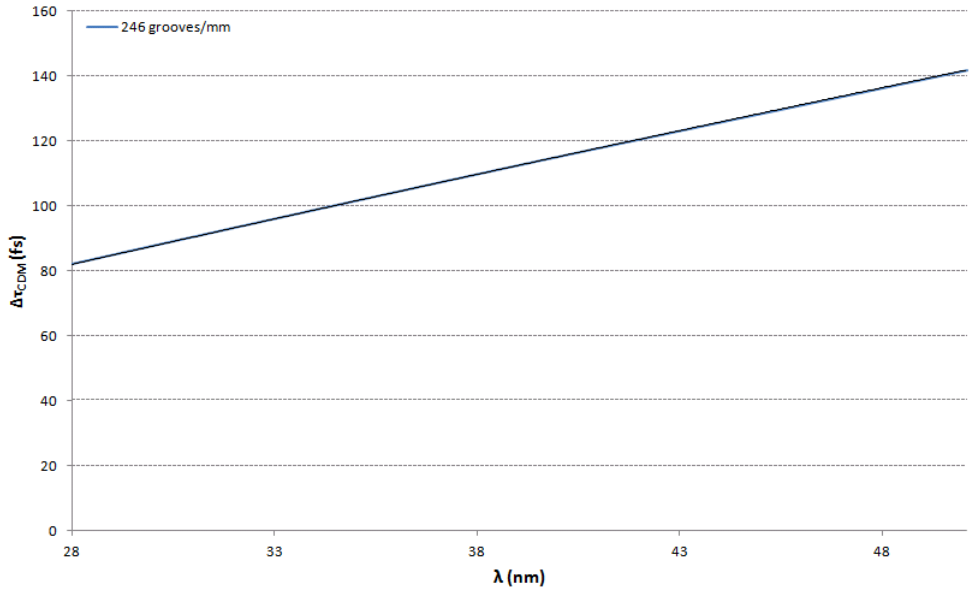

Figure 4.27: FWHM pulse front-tilt with 4-mrad full divergence, for 246 gr/mm grating, in the 25-45 eV (27.5-49.6 nm) spectral range.

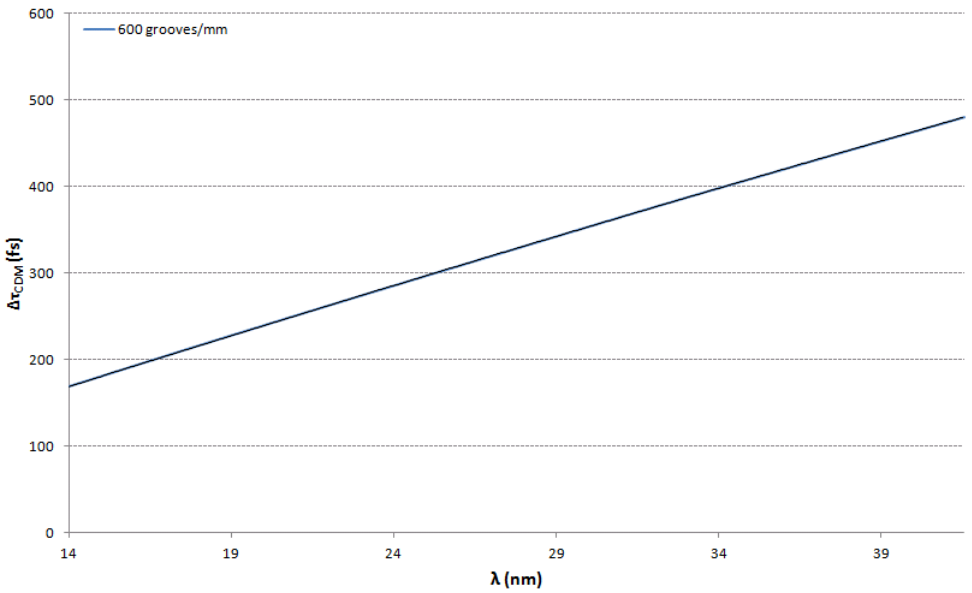

Figure 4.28: FWHM pulse front-tilt with 4-mrad full divergence, for 600 gr/mm grating, in the 30-90 eV (13.77-41.33 nm) spectral range.

Chapter 5

Labview software for remote control

Remote control for the two-axis motor rotation and gratings selection, has been done using Labview: a visual programming language from National Instruments (NI).
On the program running, a timed loop control with fractions of ms reports the slit support for gratings rotation and position. The setting-up of two limit switches is necessary to avoid the slit impact on the two toroidal mirrors. Only with a dedicate key "expert users" can change the values of the two limit switches.
We have the possibility to move (by rotation and translation of the gratings) in a specific position (with an error in rotation and translation of about 0.1° and 100 μm, respectively); or shift from the initial position of a specific value (in mm or degrees).
With Labview is even possible to perform a remote control of the Picoammeter (from Keithley) with the VISA interface control for Labview (always given by NI), through the GPIB (General Purpose Interfce Bus) standard.
I have implemented the possibillity of measuring the current with a preselected time interval of acquisition, for a fixed position (see Fig. 5.1): this function is adopted when we want to maximize the photon flux: for example, in the case of the optimization of the alignment in the XUV using the 0 order diffraction.

The second function which implemented is an automatic scanning (see Fig. 5.2) of an interval of grating's rotation angles with a pre set-up of the:

- Scan starting and ending angles;
- Interval of time in wich the grating has to stay in every scanning angle;
- Slit rotation (in degrees) for every step.

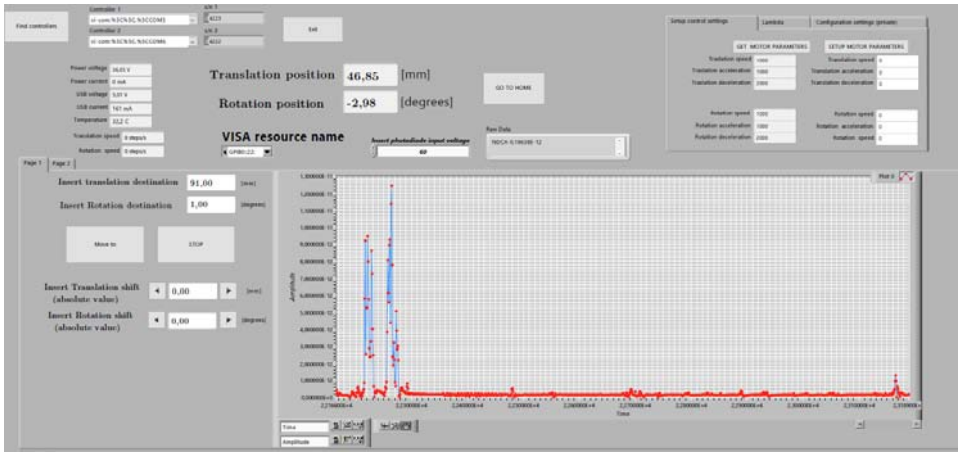

Figure 5.1: Continue measuring of current with a little time delay between two consecutive aquisitions.

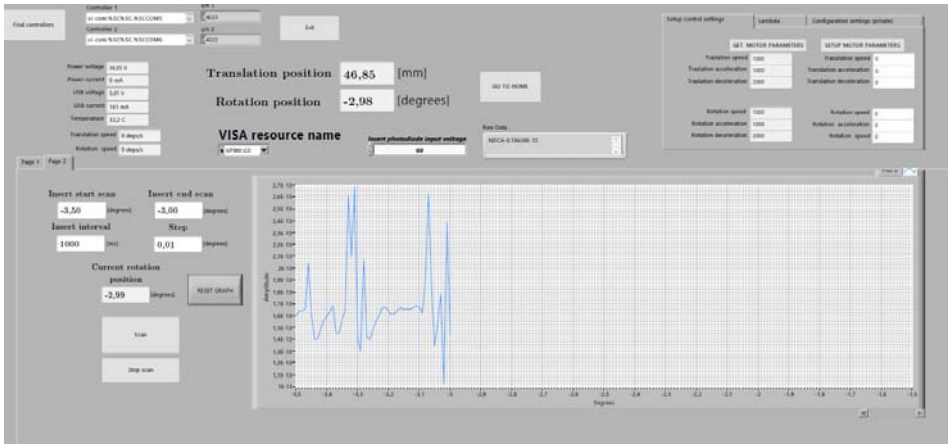

Figure 5.2: Measuring of current during a scan between two defined angles, with pre-selected time delay (in ms) and step value (in degrees) of the grating rotation.

The structure of the for loop implemented for the scanning function is reported in Fig. 5.3.

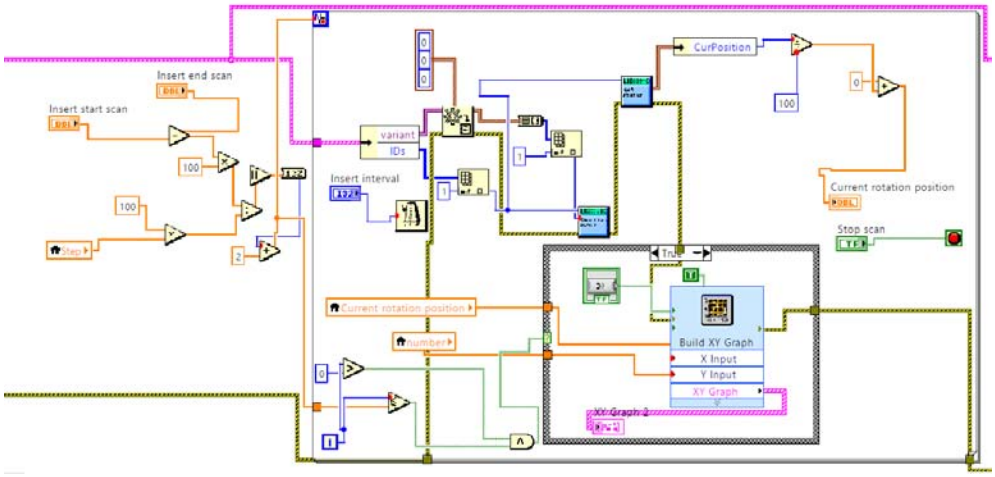

Figure 5.3: Structure of the for loop in the Labview block diagram window, which is the core of the scanning function.

Appendices

Appendix A

Generic optical system design

UV spectrum is the region of the electromagnetic spectrum which extends from about 400 nm to about 10 nm.
More specifically: Near UltraViolet (NUV) comprises wavelength from 400 nm to 300 nm, Middle UltraViolet (MUV) from 300 to 200 nm, Far UltraViolet (FUV) from 200 nm to 120 nm and eXtreme UltraViolet (XUV) comprises wavelength from 120 nm to 10 nm. Due to high absorption of air below to 200 nm the region from 200 nm to 10 nm is also called Vacuum UltraViolet because radiation can propagate only in vacuum.
X-ray region is the region of the electromagnetic spectrum which extends from about 10 nm to 0.01 nm. X-rays from about 10 nm to 0.1 nm are classified as soft X-rays, and from about 0.1 nm to 0.01 nm as hard X-rays, due to their penetrating abilities (See Fig. A.1).

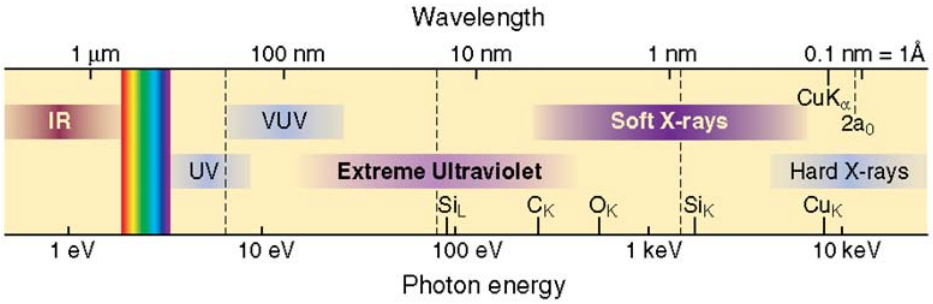

Figure A.1: UV and X-ray electromagnetic spectrum. XUV and Soft X-ray region are observable.

Spectroscopy in any spectral region requires the use of optical components that disperse the radiation into a spectrum, detect and focus light to form images.
In visible and IR spectroscopy both prisms an gratings can be used for this purpose but at wavelengths ranging from XUV to X-ray only reflective gratings are available because it is impossible to work in transmission. For the same reason, it is not possible to use lenses in this spectral domain.
XUV and soft X-ray are particular regions of the spectrum because no refractive materials transmit radiation of this wavelengths and it results also necessary working at grazing incidence because of the low reflection efficiency in normal incicence (very low under 30 nm). In Fig. A.2 the platinum reflectivity at normal and grazing incidence for these regions is reported.

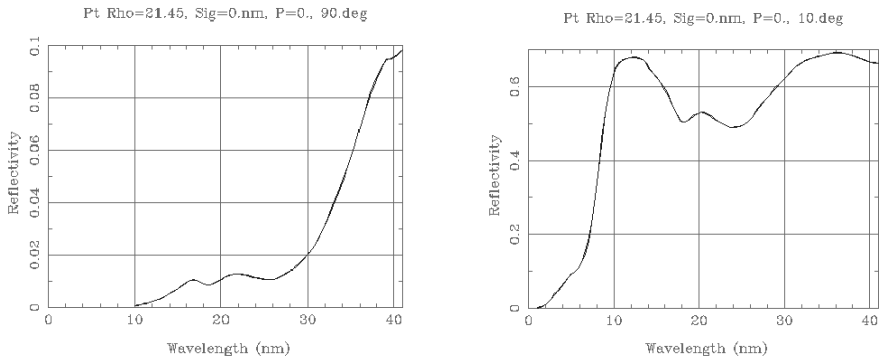

(a) Normal incidence. **(b)** Grazing incidence.

Figure A.2: Platinum mirror reflectivity.

Most used materials as coatings for mirrors in grazing incidence are: Au, Pt, s-C, Ni, their reflectivity are reported in Fig. A.3.
An XUV source (with a shutter) emits radiation in a large emission cone; a slit that define a preferential direction of acceptance of radiation is usually placed after the source: it limits the beam propagation angle towards the next element; then a monochromator select a specific wavelength in the XUV domain; finally a grazing incidence mirrors system focuses light in the sample (for absorption measurements etc.) - see Fig. A.4.

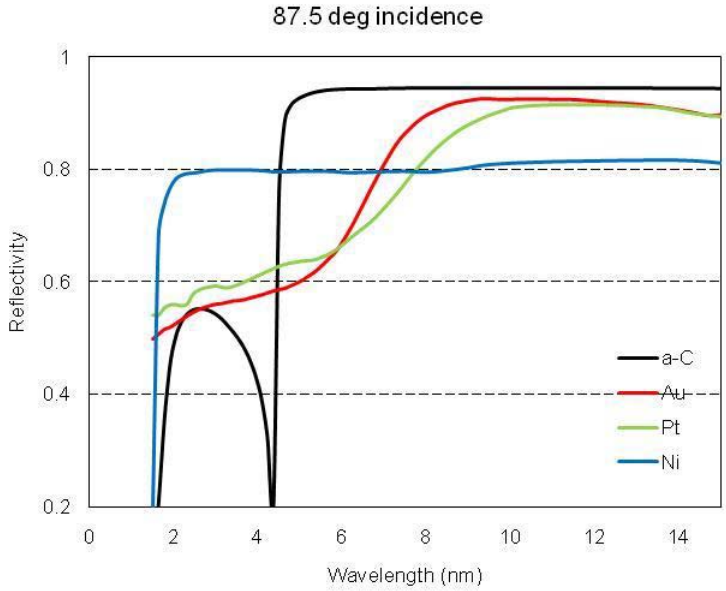

Figure A.3: Reflectivity for different materials in grazing incidence.

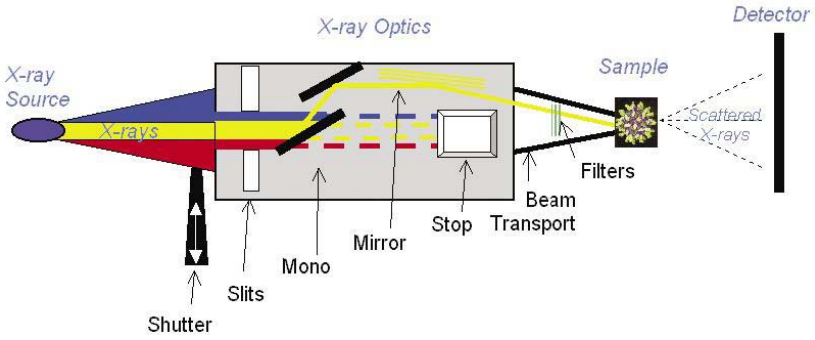

Figure A.4: Generic optical system in the XUV domain.

Appendix B

Aberrations

Aberrations are deformations and distortions of the shape of the image (focus) produced by an optical system which cause a decay of image quality after an optical system.
The main purpose of an optical system is create a no aberration image.
A spherical surface (mirror or lens) focuses all rays in a point without aberrations only for little angles of propagation (relying on paraxial theory), indeed for angles $\theta \leq 30°$ we can linearize and approximate sin function having:

$$sin\theta \simeq \theta - \frac{\theta^3}{3!} + \frac{\theta^5}{5!} - \frac{\theta^7}{7!} + \ldots \simeq \theta \tag{B.1}$$

If we aren't in paraxial conditions and we use spherical mirrors (less expensive and easily to realize), we have aberrations presence.
There are three main types of aberrations:

- **Astigmatism:** Considering a lens, and instead light it normally (where we don't have aberrations), we illuminate it with an angle φ respect to normal; we can see two different curvature radiuses in the sagittal and tangential directions (and we see an ellipse), so we can see two different spheres in the two directions, and spheres with different radiuses focus in different points.
  So a point will not be focalize in another point, but we see a vertical or horizontal line, if we observe, respectively in the tangential or sagittal focus, and a circumference for the other points (Fig. B.1).

If we want to correct astigmatism we have to use cylindrical lenses, for moving only one of the two focuses.

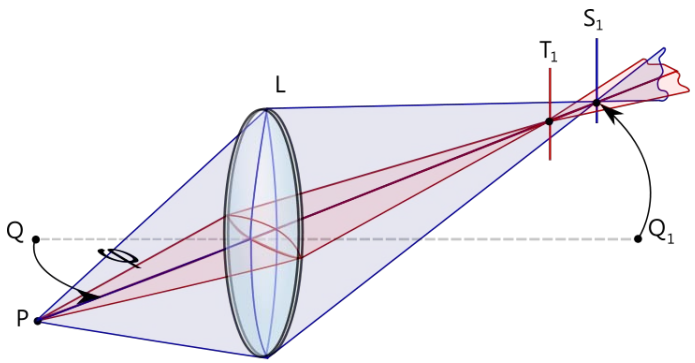

Figure B.1: Astigmatism. Two focal lengths are observable, one for the tangential rays (T) and one for the sagittal rays (S), in which the cone of rays focuses in two orthogonal segments.

- **Spherical aberration:** While paraxial rays propagate and focus in a single point, for rays with larger angles we can't approximate sin function with it's angle, and they focus in different points.

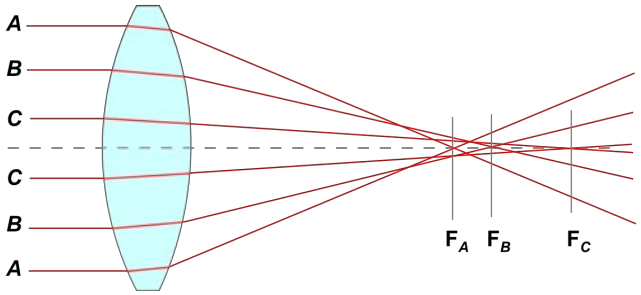

Figure B.2: Spherical aberration. It is observable the dependence of the focal length on aperture for non paraxial rays. Rays striking the surface at greater distance from the axis are focused nearer the vertex.

When we look at a ray beam passing through a lens, it is easy to understand that its focal plan depends on the distance from the optical axis. With a spherical surface, lens or mirror, incoming rays

from differents heigths from the axis do not bend at the same position and focus at slightly different distance along the axis.
So, if the center of the image stay in focus an bright, the edges of the field appear blurry and dimmer as in Fig. B.2.

- **Coma aberration.** It arises from the fact that the transverse magnification differs for rays striking off-axis regions of the mirrors. The net result is that an off-axis object point is imaged in a geometrical figure which somewhat resembles the shape of a comet, a coma (see Fig. B.3). The figure of aberration is observable if the object is not at infinite, but the aperture of the bundle of rays must prevail over its inclination.

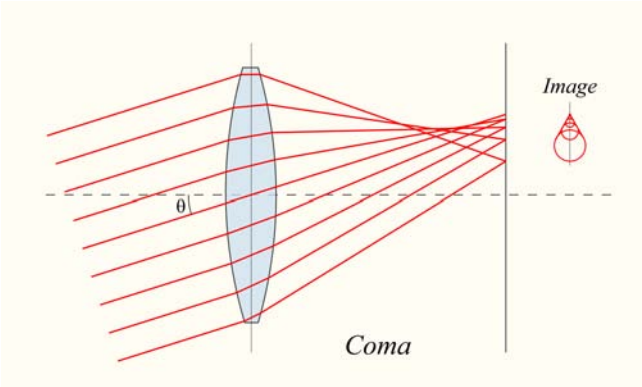

Figure B.3: Coma. An off-axis object point is imaged in a geometrical figure which somewhat resembles the shape of a coma.

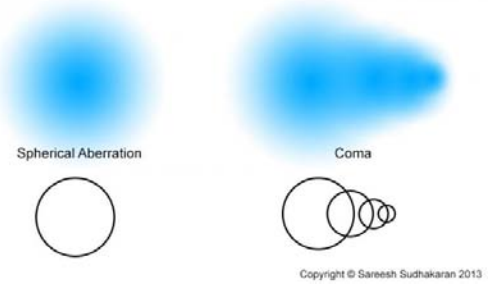

Figure B.4: Spherical and coma aberraions.

Appendix C

Spherical and toroidal mirrors

We have to consider two equations for a mirror (Fig. C.1), considering that we have two planes: tangential and sagittal.

$$tangential\ \ plane \quad \frac{1}{p}+\frac{1}{q}=\frac{2}{Rcos\alpha} \tag{C.1}$$

$$tangential\ \ plane \quad \frac{1}{p}+\frac{1}{q'}=\frac{2cos\alpha}{\rho} \tag{C.2}$$

where, α is the beam incidence angle respect to the normal of the mirror, p is the source-mirror distance; q and q' are, respectively, the mirror-image distance in the tangential and sagittal plane; and R and ρ are, respectively, the two tangential and sagittal curvature radius.

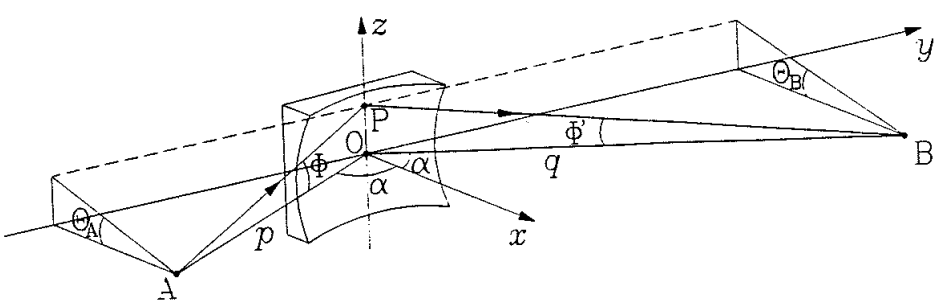

Figure C.1: Tangential plane of a mirror.

For a **spherical mirror** $R = \rho$, and in this case we have always astigmatism when $\alpha \neq 0$ (the case α is insignificant for the beam propagation). Considering a spherical mirror in grazing incidence, in the horizontal (tangential) plane we see the curvature radius of the sphere, having a point focus after the mirror; but in the sagittal plane we see a vertical plane mirror and we cannot have a focus; the result after the mirror is a line in the vertical (sagittal) plane. **So, rays in the sagittal plane propagate as if we have a plane mirror. A point is focus in a line.**

Alternatively, for a **toroidal mirror** (Fig. C.2), we have R $\neq \rho$ and we can put q = q', obtaining a stigmatic mirror. From the equations (C.1) and (C.2) we obtain the equation:

$$\frac{\rho}{R} = cos^2\alpha \tag{C.3}$$

We can use a toroidal mirror in grazing incidence with p = q = q' = $Rcos\alpha$ (**Rowland mounting**). in this case, as demonstrated by Rowland we don't have coma aberration, and the magnification M = p/q is unitary.

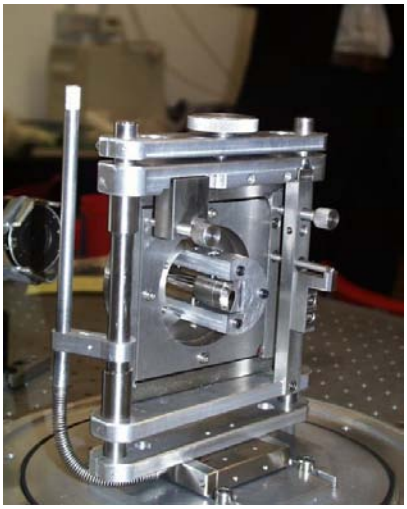

Figure C.2: Platinum toroidal mirror.

Appendix D

Grazing incidence diffraction gratings

D.1 Diffraction

Geometrical treatment for rays propagation is valid for the aberrations compensation, but we cannot consider the diffraction pheneomenon.
If we wanto to consider diffraction we can't consider light propagation with it's k wave vector obeying to Snell laws at every interface change, but we have to consider light for it's ondulatory nature.
For example, if we consider a **slit**, when the aperture of a slit become narrow (comparable with the beam wavelength), light spreads: this because of the presence of diffraction and we have to consider light propagation, not in a straight way, but as a wave.
Two are the main types of diffraction:

- **Fraunhofer:** The source that causes diffraction is put at infinite distance.
- **Fresnel:** The source that causes diffraction is put at finite distance.

When a beam of light is partly blocked by an obstacle, some of the light is scattered around the object, and light and dark bands are often seen at the edge of the shadow; this effect is known as diffraction. These effects can be modelled using the **Huygens–Fresnel** principle. Huygens postulated that every point on a primary wavefront acts as a source of

spherical secondary wavelets and the sum of these secondary waves determines the form of the wave at any subsequent time. Fresnel developed an equation using the Huygens wavelets together with the principle of superposition of waves, which models these diffraction effects quite well. It is not a straightforward matter to calculate the displacement given by the sum of the secondary wavelets, each of which has its own amplitude and phase, since this involves addition of many waves of varying phase and amplitude. When two waves are added together, the total displacement depends on both the amplitude and the phase of the individual waves: two waves of equal amplitude which are in phase give a displacement whose amplitude is double the individual wave amplitudes, while two waves which are in opposite phases give a zero displacement. Generally, a two-dimensional integral over complex variables has to be solved and in many cases, an analytic solution is not available.

D.1.1 Fraunhofer diffraction

The Fraunhofer diffraction equation is a simplified version of the Kirchhoff's diffraction formula and it can be used to model the light diffracted when both the light source and the viewing plane are effectively at infinity with respect to the diffracting aperture. In this case, the incident light is a plane wave so that the phase of the light at each point in the aperture is the same. The phase of the contributions of the individual wavelets in the aperture varies linearly with position in the aperture, making the calculation of the sum of the contributions relatively straightforward in many cases. Strictly speaking, the Fraunhofer approximation only applies when the diffracted pattern is viewed at infinity, but in practice it can be applied in the far field ($L \gg \frac{W^2}{\lambda}$, where L is the distance of the of the target and W is the aperture or slit size), and also in the focal plane of a positive lens.

- **Rectangular slit with infinite width:** Every point of the slit can be considered as a secondary source of a spherical wave, so in the different points of the target we have light or dark fringes depending on a superposition of in-phase waves or not, as in Fig. D.1.

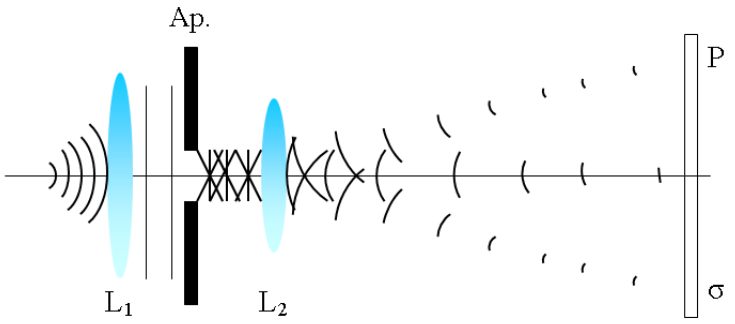

Figure D.1: Fraunhofer diffraction from a single rectangular slit of infinite depth. The first lens (i.e. parabolic) creates the condition of an infinite distance source from the slit, and the second lens focus the diffracted rays in a target. The result on the target is an alternation of light and dark fringes, which indicate the presence of constructive or destructive interference.

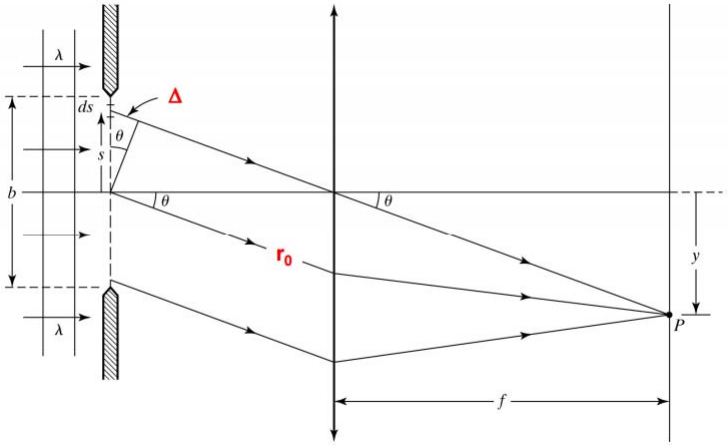

Figure D.2: Emission by all the secondary spherical sources at angle θ.

Considering a mathematical treatment (Fig. D.2), for every single secondary spherical wave emitted by the slit we have the electric field in a point P:

$$dE_p = \left(\frac{dE_0}{r}\right) e^{i(kr-\omega t)} \tag{D.1}$$

and, for every interval ds at distance s from the slit center:

$$\begin{aligned} dE_p &= \left(\frac{dE_0}{r_0+\Delta}\right) e^{i[k(r_0+\Delta)-\omega t]} \cong \left(\frac{dE_0}{r_0}\right) e^{i[k(r_0+\Delta)-\omega t]} \\ &= \left(\frac{E_L ds}{r_0}\right) e^{i[kr_0+kssin\theta-\omega t]} \end{aligned} \tag{D.2}$$

In the first approximation of the Eq. (D.1) we can neglect the amplitude term Δ at denominator, but we can't neglect it in phase because we are treating with nm wavelengths, and finally we obtain for the irradiance a sinc (see Fig. D.3) function:

$$I_p = I_0 sinc^2\beta = I_0 \frac{sin^2\beta}{\beta^2} \tag{D.3}$$

Where $I_0 = \frac{\epsilon_0 c}{2}$ and $\beta = \frac{1}{2}kbsin\theta$.

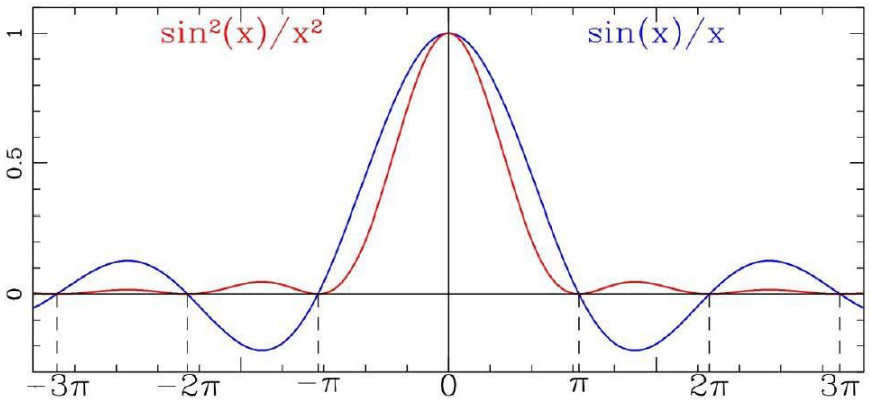

Figure D.3: Irradiance (red) and electric field (blue) from a single rectangular slit with infinite width. We have irradiance maximum when $\beta = 0$ and zeros when $\beta = m\pi$ (with m relative integer different from zero).

The width of the central maximum is (see Fig. D.4):

$$\Delta\theta = \frac{2\lambda}{b} \Rightarrow W = \frac{2L\lambda}{b} \tag{D.4}$$

so, more b is small and Lλ is big, and more W increases.

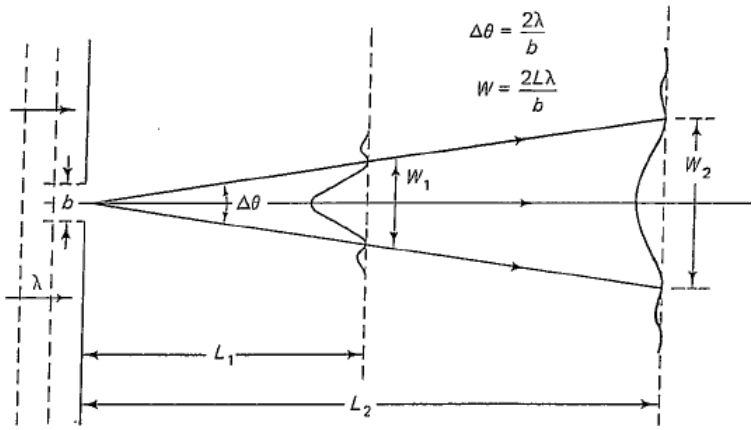

Figure D.4: Angular and linear width of the central maximum diffraction.

- **Rectangular fenditure:** Appling again Huygens-Fresnel principle for horizontal and vertical directions we obtain (see Fig. D.5):

$$I = I_0 sinc^2 \alpha sinc^2 \beta \tag{D.5}$$

with $\alpha = \frac{1}{2} ka sin\theta$ and $\beta = \frac{1}{2} kb sin\theta$.

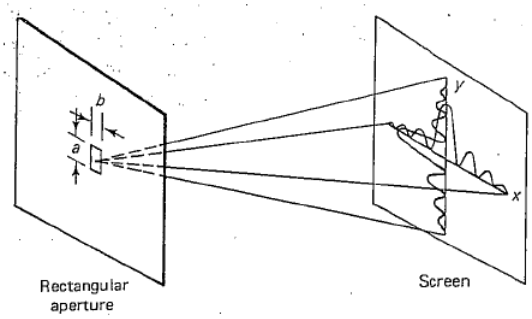

(a) Rectangular slit with finite horizontal and vertical dimensions.

(b) Image obtained in a screen by a finite dimensions rectangular slit

Figure D.5: Rectangular slit with finite dimensions.

- **Pin-hole:** A pin-hole is a circular slit; in this case we have to integrate the electric field considering every rectangular slit inside the pin-hole, obtaining an irradiance:

$$I = I_0 \left(\frac{2J_1(\gamma)}{\gamma} \right)^2 \tag{D.6}$$

where, $J_1(\gamma)$, with $\gamma = \frac{K}{2} D sin\theta$ (D = pin-hole diameter) is the first order Bessel function (see Fig. D.6).

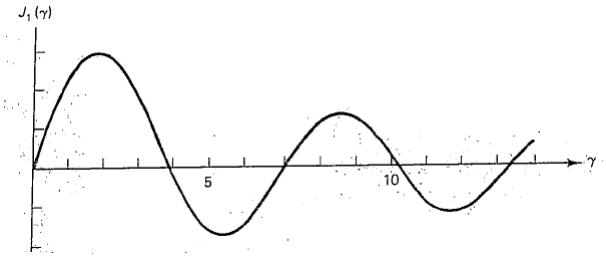

(a) First order Besssel function $J_1(\gamma)$.

(b) Pin-hole diffraction on a screen.

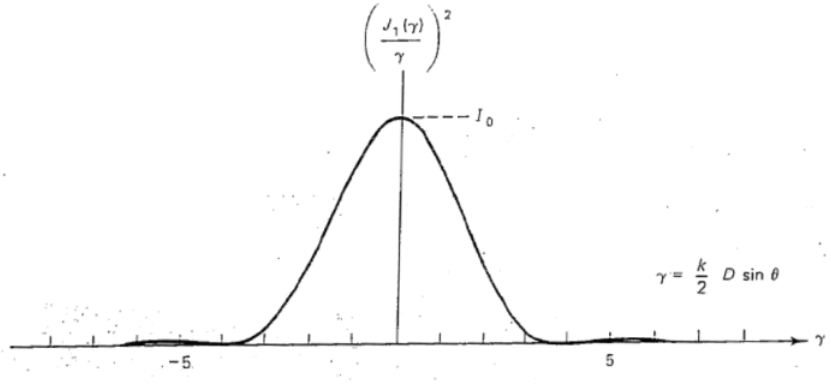

(c) Pin-hole irradiance.

Figure D.6: Pin-hole functions.

In this case the width of the central maximum is:

$$\Delta\theta = \frac{1.22\lambda}{D} \Rightarrow W = \frac{1.22\lambda L}{D} \tag{D.7}$$

Working in the XUV and soft X-ray region with small wavelengths (tens of nm), seeing equations our image is not blurry by diffraction effect but, most commonly by aberrations effect, so we have to correct them.

- **Double slit and multiple slits:** In this case (Fig. D.7 - D.8) we have to envelope (product) two electric field functions: the one associated to the two slit contribute and the other one to a single slit:

$$I = 4I_0 \left(\frac{sin\beta}{\beta} \right)^2 cos^2\alpha \tag{D.8}$$

where, $\beta = \frac{1}{2}kbsin\theta$ and $\alpha = \frac{1}{2}kasin\theta$

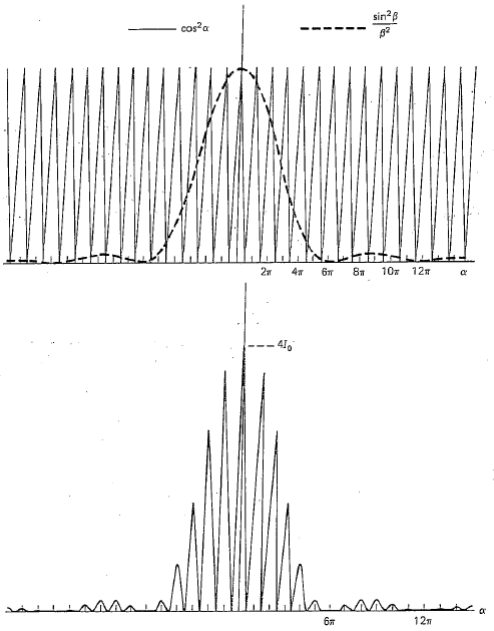

(a) Envelope of the two functions associated to a single and two slits.

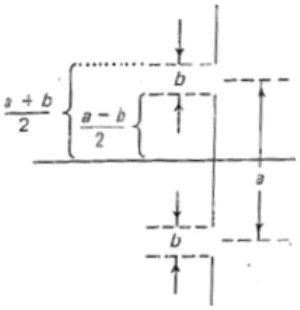

(b) Double slit schematic.

Figure D.7: Double slit functions.

Similarly, for multiple slits, we have:

$$I = I_0 \left(\frac{sin\beta}{\beta} \right)^2 \left(\frac{sinN\alpha}{sin\alpha} \right)^2 \tag{D.9}$$

and, we have a maximum when:

$$asin\theta = m\lambda \tag{D.10}$$

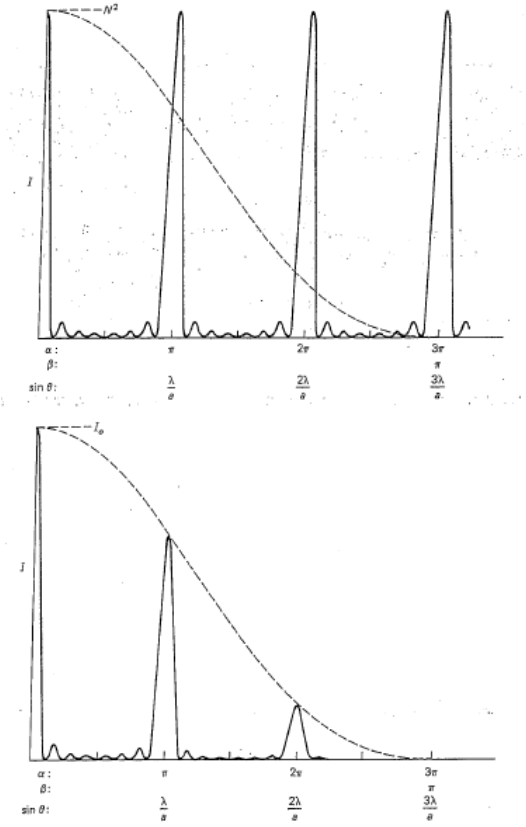

Figure D.8: Multiple slits diffraction irradiance, envelope of the two functions associated to a single and multiple slits.

- **Grating:** If we have a very large number N of periodic slits (thousands), each one with width b and spaced a; we can consider two adjacent slits, and we have an optical path difference that is:

$$\Delta = \Delta_1 + \Delta_2 = asin\theta_i + asin\theta_m \tag{D.11}$$

having θ_i and θ_m, respectively the incidence and diffraction angles.

In this case, if we want to have constructive interference the contribution given by two adjacent slits have to be a 2π multiple in phase, or a wavelength multiple in the optical path (Fig. D.9). Then we have the **grating equation**:

$$a\,(sin\theta_i + sin\theta_m) = m\lambda \tag{D.12}$$

with m relative integer number.

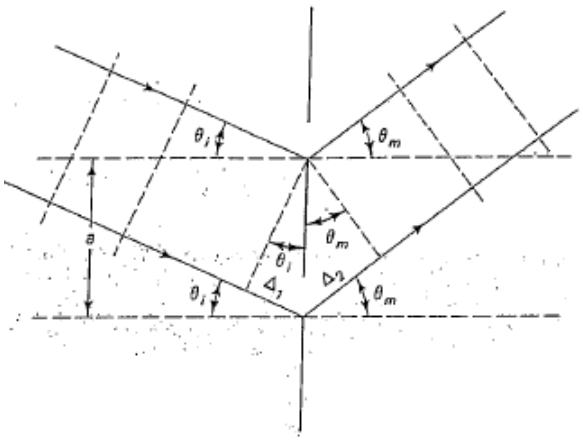

Figure D.9: Diffraction grating optical path difference between two adjacent slits.

D.2 Diffraction gratings equations

Instead of a transmission grating, we can make a reflection grating, when in a surface we produce a sequence of periodic grooves; and is still valid the grating Eq. (D.12):

$$sin\alpha + sin\beta = m\lambda\sigma \tag{D.13}$$

when α and β are, respectively the incidence and diffraction angles referred to the normal of the grating; and $\sigma = \frac{1}{d}$ (where d is the groove spacing) is the number of lines (grooves)/mm - we can have from hundreds to thousands grooves/mm.
If the entrance beam is a polychromatic light; its different wavelengths will be diffracted at different diffraction angles.
Diffraction by a grating can be visualized from the geometry in Fig. D.10, which shows a light ray incident at an angle a and diffracted by a grating along at set of angles β_m. These angles are measured from the grating normal, which is shown as the dashed line perpendicular to the grating surface at its center.
The sign convention for these angles depends on whether the light is diffracted on the same side or the opposite side of the grating as the incident light. Angles $\alpha > 0$ and $\beta_1 > 0$ (since they are measured counterclockwise from the grating normal) while the angles $\beta_0 < 0$ and $\beta_{-1} < 0$ (since they are measured clockwise from the grating normal).

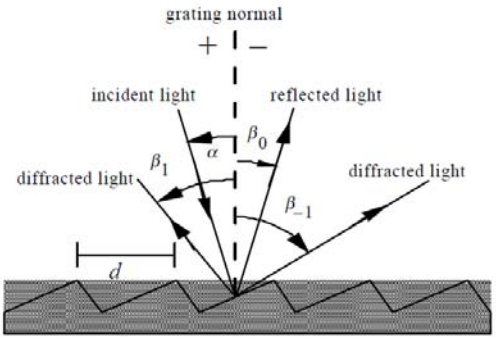

Figure D.10: A reflection grating. Sign convention and incidence and diffracted beams.

Another illustration of grating diffraction, using wavefronts (surfaces of constant phase), is shown in Fig. D.11.

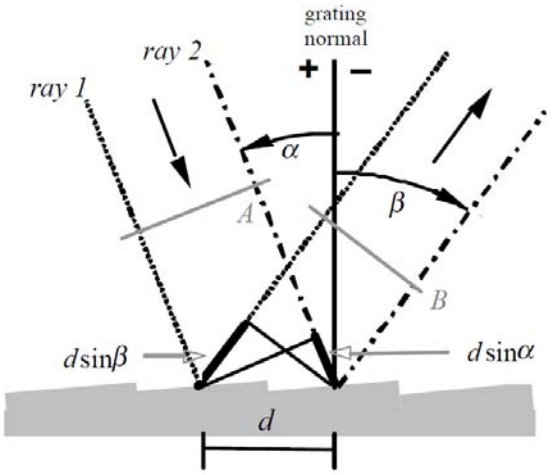

Figure D.11: Geometry of diffraction, for planar wavefronts. Two parallel rays, labeled 1 and 2, are incident on the grating one groove spacing d apart and are in phase with each other at wavefront A. Upon diffraction, the principle of constructive interference implies that these rays are in phase at diffracted wavefront B if the difference in their path lengths, $dsin\alpha + dsin\beta$, is an integral number of wavelengths; this in turn leads to the grating equation.

Eq. (D.13) is the common forms of the grating equation, but its validity is restricted to cases in which the incident and diffracted rays lie in a plane which is perpendicular to the grooves (at the center of the grating). The majority of grating systems fall within this category, which is called classical (or in-plane) diffraction. If the incident light beam is not perpendicular to the grooves, though, the grating equation must be modified:

$$\sigma m\lambda = cos\epsilon\,(sin\alpha + sin\beta) \tag{D.14}$$

Here ϵ is the angle between the incident light path and the plane perpendicular to the grooves at the grating center (the plane of the page in Fig. D.11). If the incident light lies in this plane, $\epsilon = 0$ and Eq. (D.14) reduces to the more familiar Eq. (D.13). In geometries for which $\epsilon \neq 0$,

the diffracted spectra lie on a cone rather than in a plane, so such cases are termed conical diffraction.
For a grating of groove spacing d, there is a purely mathematical relationship between the wavelength and the angles of incidence and diffraction. In a given spectral order m, the different wavelengths of polychromatic wavefronts incident at angle α are separated in angle:

$$\beta(\lambda) = sin^{-1}\left(\frac{m\lambda}{d} - sin\alpha\right) \tag{D.15}$$

When m = 0, the grating acts as a mirror, and the wavelengths are not separated ($\beta = -\alpha$ for all λ); this is called specular reflection or simply the zero order.
A special but common case is that in which the light is diffracted back toward the direction from which it came (i.e., $\alpha = \beta$); this is called the Littrow configuration, for which the grating equation becomes:

$$m\lambda = 2dsin\alpha \tag{D.16}$$

In many applications a constant-deviation monochromator mount is used, in which the wavelength λ is changed by rotating the grating about the axis coincident with its central ruling, with the directions of incident and diffracted light remaining unchanged. The deviation angle 2ζ between the incidence and diffraction directions (also called the angular deviation) is:

$$2\zeta = \alpha - \beta = constant \tag{D.17}$$

while the scan angle ϕ, which varies with λ and is measured from the grating normal to the bisector of the beams, is:

$$2\phi = \alpha + \beta \tag{D.18}$$

Note that ϕ changes with λ (as do α and β). In this case, the grating equation can be expressed in terms of ϕ and the half deviation angle ζ as:

$$m\lambda = 2dcos\zeta sin\phi \tag{D.19}$$

This version of the grating equation is useful for monochromator mounts. For the constant-deviation monochromator mount, the incidence and diffraction angles can be expressed simply in terms of the scan angle ϕ and the half-deviation angle ζ via:

$$\alpha(\lambda) = \phi(\lambda) + \zeta \tag{D.20}$$

and

$$\beta(\lambda) = \phi(\lambda) - \zeta \tag{D.21}$$

where we show explicitly that α, β and ϕ depend on the wavelength λ. For a particular groove spacing d, wavelength λ and incidence angle α, the grating Eq. (D.13) is generally satisfied by more than one diffraction angle β. In fact, subject to restrictions discussed below, there will be several discrete angles at which the condition for constructive interference is satisfied. The physical significance of this, is that the constructive reinforcement of wavelets diffracted by successive grooves merely requires that each ray be retarded (or advanced) in phase with every other; this phase difference must therefore correspond to a real distance (path difference) which equals an integral multiple of the wavelength. This happens, for example, when the path difference is one wavelength, in which case we speak of the positive first diffraction order (m = 1) or the negative first diffraction order (m = –1), depending on whether the rays are advanced or retarded as we move from groove to groove. Similarly, the second order (m = 2) and negative second order (m = –2) are those for which the path difference between rays diffracted from adjacent grooves equals two wavelengths.

The grating equation reveals that only those spectral orders for which $|\mathrm{m}\lambda/\mathrm{d}| < 2$ can exist; otherwise, $|sin\alpha + sin\beta| > 2$, which is physically meaningless. This restriction prevents light of wavelength λ from being diffracted in more than a finite number of orders. Specular reflection (m = 0) is always possible; that is, the zero order always exists (it simply requires $\beta = -\alpha$). In most cases, the grating equation allows light of wavelength λ to be diffracted into both negative and positive orders

as well. Explicitly, spectra of all orders m exist for which:

$$-2d < m\lambda < 2d, \quad m \ integer. \tag{D.22}$$

For $\frac{\lambda}{d} \ll 1$, a large number of diffracted orders will exist.
As seen from Eq. (D.13), the distinction between negative and positive spectral orders is that (see Fig. D.12):

- $\beta > -\alpha$ for positive orders (m > 0),
- $\beta < -\alpha$ for negative orders (m < 0),
- $\beta = -\alpha$ for specular reflection (m $= 0$).

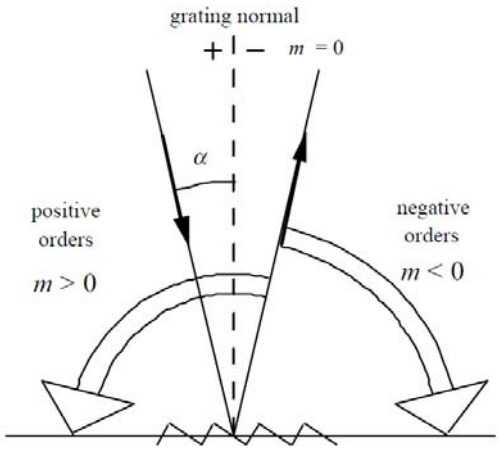

Figure D.12: Sign convention for the spectral order m.

The most troublesome aspect of multiple order behavior is that successive spectra overlap, as shown in Fig. D.13. It is evident from the grating equation that light of wavelength λ diffracted by a grating along direction b will be accompanied by integral fractions $\frac{\lambda}{2}$, $\frac{\lambda}{3}$, etc.; that is, for any grating instrument configuration, the light of wavelength λ diffracted in the m $= 1$ order will coincide with the light of wavelength $\frac{\lambda}{2}$ diffracted in the m $= 2$ order, etc. This superposition of wavelengths, which would lead to ambiguous spectroscopic data, is inherent in the grating equation itself and must be prevented by suitable filtering (called order sorting), since the detector cannot generally distinguish between light of different wavelengths incident on it (within its range of sensitivity).

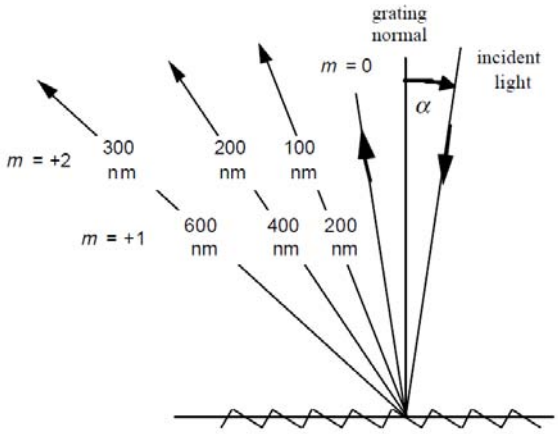

Figure D.13: Overlapping of spectral orders. The light for wavelengths 100, 200 and 300 nm in the second order is diffracted in the same direction as the light for wavelengths 200, 400 and 600 nm in the first order.

Features of diffraction gratings

The angular spread $\Delta\beta$ of a spectrum of order m between the wavelength λ and $+\Delta\lambda$ can be obtained by differentiating the grating equation, assuming the incidence angle α to be constant. The change $\Delta\beta$ in diffraction angle per unit wavelength is called **angular dispersion** and is, therefore:

$$\Delta\beta = \frac{d\beta}{d\lambda} = \frac{m\sigma}{cos\beta} \tag{D.23}$$

The **resolving power R** of a grating is a measure of its ability to separate adjacent spectral lines of average wavelength λ. It is usually expressed as the dimensionless quantity:

$$R = \frac{\lambda}{\Delta\lambda} \tag{D.24}$$

where $\Delta\lambda$ is the limit of resolution, the difference in wavelength between two lines of equal intensity that can be distinguished.

The theoretical resolving power of a planar diffraction grating is given by the equation:

$$R = mN \tag{D.25}$$

where N is the total number of grooves illuminated on the surface of the grating.

While resolving power can be considered a characteristic of the grating and the angles at which it is used, the ability to resolve two wavelengths λ_1 and $\lambda_2 = \lambda_1 + \Delta\lambda$, generally depends not only on the grating but on the dimensions and locations of the entrance and exit slits (or detector elements), the aberrations in the images, and the magnification of the images. The minimum wavelength difference $\Delta\lambda$ between two wavelengths that can be resolved unambiguously, a quantity called **resolution**, can be determined by convoluting the image of the entrance aperture (at the image plane) with the exit aperture (or detector element). This measure of the ability of a grating system to resolve nearby wavelengths is arguably more relevant than is resolving power, since it takes into account the image effects of the system. While resolving power is a dimensionless quantity, resolution has spectral units (usually nanometers).

The distribution of power of a given wavelength diffracted by a grating into the various spectral order depends on many parameters, including the power and polarization of the incident light, the angles of incidence and diffraction, the (complex) index of refraction of the materials at the surface of the grating, and the groove spacing. A complete treatment of grating effciency requires the vector formu- lation of electromagnetic theory (i.e., Maxwell's equations) applied to corrugated surfaces, which has been studied in detail over the past few decades. While the theory does not yield conclusions easily, certain rules of thumb can be useful in making approximate predictions. The simplest and most widely used rule of thumb regarding grating effciency (for reflection gratings) is the blaze condition:

$$m\lambda_{blaze}\sigma = 2sin\theta_B \tag{D.26}$$

where θ_B (called the blaze angle of the grating) is the angle between the face of the groove and the plane of the grating (see Fig. D.14).

When the blaze condition is satisfied, effciency is enhanced [24].

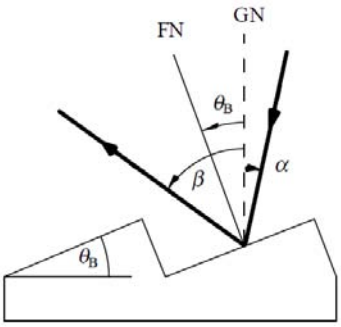

Figure D.14: Blaze condition. The angles of incidence α and diffraction β are shown in relation to the facet angle θ_B for the blaze condition. GN is the grating normal and FN is the facet normal. When the facet normal bisects the angle between the incident and diffracted rays, the blaze condition is satisfied.

Eq. (D.26) generally leads to the highest efficiency when the following condition is also satisfied:

$$2\zeta = \alpha - \beta = 0 \tag{D.27}$$

Equations (D.26) and (D.27) collectively define the *Littrow blaze condition*. When Eq. (D.27) is not satisfied (i.e., $\alpha \neq \beta$ and therefore the grating is not used in the Littrow configuration), efficiency is generally seen to decrease as one moves further off Littrow (i.e., as $|2\zeta|$ increases).

Bibliography

[1] K. Midorikawa, “High-Order Harmonic Generation and Attosecond Science,” Japanese J. Appl. Phys., 50 (2011).

[2] Martin E. Fermann,Almantas Galvanauskas,Gregg Sucha "Ultrafast Lasers: Technology and Applications", 2005.

[3] T. Sekikawa, T. Okamoto, E. Haraguchi, M. Yamashita, and T. Nakajima, “Two-photon resonant excitation of a doubly excited state in He atoms by high-harmonic pulses,” Opt. Express 16(26), 21922–21929 (2008).

[4] P. Villoresi, “Compensation of optical path lengths in extreme-ultraviolet and soft-x-ray monochromators for ultrafast pulses,” Appl. Opt. 38, 6040-6049 (1999).

[5] L. Poletto and P. Villoresi, “Time-compensated monochromator in the off-plane mount for extreme-ultraviolet ultrashort pulses,” Appl. Opt. 45, 8577–8585 (2006).

[6] L. Poletto, P. Villoresi, F. Frassetto, F. Calegari, F. Ferrari, M. Lucchini, G. Sansone, M. Nisoli, “Time-delay compensated monochromator for the spectral selection of extreme-ultraviolet high-order laser harmonics,” Rev. Sci. Instrum. 80, 123109 (2009).

[7] M. Ito, Y. Kataoka, T. Okamoto, M. Yamashita, and T. Sekikawa, “Spatiotemporal characterization of singleorder high harmonic pulses from time-compensated toroidal-grating monochromator,” Opt. Express 18, 6071–6078 (2010).

[8] M. Lewenstein, Ph. Balcou, M. Yu. Ivanov, Anne L'Huillier, and P. B. Corkum. Theory of high-harmonic generation by low-frequency laser fields. Phys. Rev. A, 49(3):2117–2132, Mar 1994.

[9] P. B. Corkum. Plasma perspective on strong field multiphoton ionization. Phys. Rev. Lett., 71:1994–1997, Sep 1993.

[10] V. P. Krainov M. V. Ammosov, N. B. Delone. Tunnel ionization of complex atoms and atomic ions by an alternating electromagnetic field. Soviet Physics, 64(1191):1191–1194, 1986. 80, 3817–3819 (2002).

[11] V. S. Popov A. M. Perelomov and M. V. Terent'ev. Ionization of atoms in an alternating electric field. Soviet Physics Jept, 23(5):924–925, May 1966.

[12] J. B. Watson, A. Sanpera, K. Burnett, and P. L. Knight. Wave-packet recollision and pulse-shape effects in high-harmonic generation. Phys. Rev. A, 55:1224–1233, Feb 1997.

[13] S. A. Akhmanov, V. A. Vysloukh, and A. S. Chirkin, Optics of Femtosecond Laser Pulses (American Institute of Physics, 1992).

[14] W. Cash, "Echelle spectrographs at grazing incidence," Appl. Opt. 21, 710–717 (1982).

[15] R. Petit, ed., Electromagnetic Theory of Gratings (Springer- Verlag, 1980), Chap. 4, pp. 125–165.

[16] W. Werner, "X-ray efficiencies of blazed gratings in extreme off-plane mountings," Appl. Opt. 16, 2078–2080 (1977).

[17] L. Poletto, F. Frassetto, J. I. Larruquert, and J. A. Mendez, "Efficiency measurements on gratings in the off-plane mount for a high-resolution grazing-incidence XUV monochromator," Proc. SPIE 7077, 707712 (2008).

[18] L. Poletto and P. Villoresi, "Time-compensated monochromator in the off-plane mount for extreme-ultraviolet ultrashort pulses," Appl. Opt. 45, 8577–8585 (2006).

[19] L. Poletto, G. Tondello, and P. Villoresi, "Optical design of a spectrometer–monochromator for the extreme-ultraviolet and soft-x-ray emission of high-order harmonics," Appl. Opt. 42, 6367–6373 (2003).

[20] L. Poletto, S. Bonora, M. Pascolini, and P. Villoresi, "Instrumentation for analysis and utilization of extreme-ultraviolet and soft x-ray high-order harmonics," Rev. Sci. Instrum. 75, 4413–4418 (2004).

[21] W. Werner, "X-ray efficiencies of blazed gratings in extreme off-plane mountings," Appl. Opt. 16, 2078–2080 (1977).

[22] J. F. Seely, L. I. Goray, B. Kjornrattanawanich, J. M. Laming, G. E. Holland, K. A. Flanagan, R. K. Heilmann, C.-H. Chang, M. L. Schattenburg, and A. P. Rasmussen, "Efficiency of a grazing-incidence off-plane grating in the soft-x-ray region," Appl. Opt. 45, 1680–1687 (2006).

[23] L. Poletto and F. Frassetto, "Design of high-resolution grazing-incidence echelle monochromators," Appl. Opt. 48, 5363–5370 (2009).

[24] C. Palmer (2005), Diffraction Grating Handbook, Erwin Loewen Editor, New York.

Ringraziamenti

Per prima cosa, ci tengo a ringraziare i miei genitori Renato e Luigina, che da sempre mi sostengono con affetto e non mi fanno mai mancare nulla: dedico a loro questa tesi.

Desidero ringraziare anche il mio relatore, Luca Poletto, che mi sta dando la possibilità di interfacciarmi con un argomento affascinante come lo studio dei laser ultrabrevi nell'estremo ultravioletto mediante generazione di armoniche di ordine elevato, che mi permette di essere fiero del lavoro fatto in questi anni di studio.

Grazie anche a tutte le persone che mi sono vicine e che continuano a supportami (e sopportarmi).
Grazie ai "più belli" Savio, mio cugino Marco, Marco Garato, Fili, Leo, Marco Terrin, Eugenio, Luca, Simone ed Ely per i bellissimi momenti passati assieme e per farmi straviare, da anni, con la vostra simpatia e amicizia.

Grazie infine a Paolo e a Fabio per la loro pazienza e l'essenziale aiuto nella scrittura di questa tesi.

Grazie di cuore a ognuno di voi.